
Computational Study of Transition-Metal Substitutions in Rutile TiO₂ (110) for Photoelectrocatalytic Ammonia Synthesis

Benjamin M. Comer^{1†}, Max H. Lenk^{2†}, Aradhya P. Rajanala³, Emma L. Flynn⁴, Andrew J. Medford^{1*}

December 13, 2019

Abstract Synthesis of ammonia through photo- and electrocatalysis is a rapidly growing field. Titania-based catalysts are widely reported for photocatalytic ammonia synthesis and have also been suggested as electrocatalysts. The addition of transition-metal dopants is one strategy for improving the performance of titania-based catalysts. In this work, we screen *d*-block transition-metal dopants for surface site stability and evaluate trends in their performance as the active site for the reduction of nitrogen to ammonia on TiO₂. We find a linear relationship between the *d*-band center and formation energy of the dopant site, while the binding energies of N₂, N₂H, and NH₂ all are strongly correlated with the cohesive energies of the dopant metals. The activity of the metal-doped systems shows a volcano type relationship with the NH₂ and N₂H energies as descriptors. Some metals such as Co, Mo, and V are predicted to slightly improve photo- and electrocatalytic performance, but most metals inhibit the ammonia synthesis reaction. The results provide insight into the role of transition-metal dopants for promoting ammonia synthesis, and the trends are based on unexpected electronic structure factors that may have broader implications for single-atom catalysis and doped oxides.

1 Introduction

The fixation of atmospheric nitrogen has long been one of the prime challenges in chemistry and chemical engineering [64, 67]. The Haber-Bosch process has been the route of choice for performing nitrogen fixation for the past century, permitting much of the population growth over that period [74]. However, this process has significant drawbacks, including high CO₂ emissions and centralized production due to large capital requirements [8]. The Haber-Bosch process's considerable contribution to CO₂ emissions has been an increasingly pressing concern for the global community, as it accounts for 340 million tonnes of CO₂—fully 2% of the carbon emissions worldwide [27, 66]. For this reason, supplanting the Haber-Bosch process would represent a significant contribution to global efforts to curb climate change. Another drawback lies in the centralization of the Haber-Bosch process, which leads to high transportation costs and contributes to global economic inequality [8]. Due to the high pressures and pure feedstocks required, Haber-Bosch has significant economies of scale. Constructing a new plant requires significant capital and natural resources, as well as a critical mass of demand. Industrialized nations meet these criteria through a constant availability of capital and industrialized agricultural with a steady demand for fertilizer [47]. However, these barriers have prevented developing regions, such as Sub-Saharan Africa, from developing Haber-Bosch plants. The lack of local production results in high costs of fertilizers due to transportation, corresponding to reduced crop yields, which lowers demand and further increases prices [59]. This causes the fertilizer to be most expensive in regions where it is most needed.

¹ School of Chemical and Biomolecular Engineering, Georgia Institute of Technology

² School of Materials Science and Engineering, Georgia Institute of Technology

³ School of Physics, Georgia Institute of Technology

⁴ School of Computer Science, Georgia Institute of Technology

† These authors contributed equally to this work.

* Correspondence E-mail: andrew.medford@chbe.gatech.edu
311 Ferst Drive NW, Atlanta, Georgia 30318
Tel.:+1 (404) 385-5531

Due to the various drawbacks of the Haber-Bosch process, researchers have sought alternative means of producing fixed nitrogen [8, 48, 80, 38, 16, 50]. Two strategies that have received significant recent interest are electrocatalysis [48] and photocatalysis [49]. However, making either of these technologies viable presents a significant challenge. Electrochemical nitrogen fixation requires generating electricity and transporting electrons to the catalyst surface to perform the reaction [38]. The need for both solar and electrocatalytic cells may limit the viability of electrochemical processes in the developing world [8]. An alternative route is photochemical nitrogen fixation, where the catalyst is placed in direct contact with sunlight, air, and water vapor to produce fixed nitrogen. The photochemical route has the potential to operate with low capital investment and simpler infrastructure, making it promising for low-resource environments.

The scientific community has known of photochemical nitrogen fixation for decades, but inconsistent results and low rates have discouraged further study [49]. N. Dhar [17] was the first to investigate photocatalytic nitrogen, and the first well-controlled experiments were performed decades later when Schrauzer and Guth independently re-discovered the process [69]. Schrauzer and Guth were able to establish the production of NH_3 in sterilized desert sands under illumination, [69] including confirmation via isotopic labeling [70]. Numerous independent experiments have been performed over the years and reported photochemical production of NH_3 over titania materials [6, 3, 75, 41, 87, 33], though legitimate skepticism has remained due to issues with contamination [20, 14, 15], interference [22, 11], and inconsistent results [49]. However, recent experiments utilizing ambient pressure X-ray Photoelectron Spectroscopy (AP-XPS) have observed reduced nitrogen compounds under only under illumination [9]. These experiments provide direct experimental evidence that photo-induced nitrogen reduction occurs on titania surfaces, though the presence of carbon-based impurities was found to be a critical enabler of the process.

Despite improved understanding of photocatalytic nitrogen fixation, the rates of reaction on titania-based catalysts remain relatively low (μmol scale [33]). The competition of NH_3 production with H_2 evolution is a key issue for electrocatalytic or photocatalytic nitrogen fixation and has been dubbed the “selectivity challenge” [73]. For this reason, high Faradic efficiency is also often sought in the electrochemical literature [48]. The driver of this is the opportunity cost of using electricity for catalysis over other possible uses. For this reason, many electrochemical studies focus on low-

overpotentials where the selectivity is generally highest, but the overall reaction rate is relatively low.

In contrast, photo-excited electrons are difficult to harvest for alternate uses, and hence the overall solar-to-ammonia efficiency is the key metric for assessing photocatalytic ammonia production. Rates on the order of 0.02% solar-to-ammonia efficiency have been reported for pure titania catalysts [33]. These rates are orders of magnitude lower than the $\sim 20\%$ solar-to-hydrogen efficiency achieved by state-of-the-art catalytic systems for solar hydrogen production [54, 36]. However, it has been posited that a comparatively low solar efficiency of $\sim 0.1\text{-}1\%$ may be sufficient to enable solar fertilizer technology [8, 49]. With sufficiently low capital cost, this system could see use in areas that are far from fertilizer plants due to the lowering of transportation costs. Thus, strategies for enhancing the rate of photocatalytic ammonia production on titania catalysts may be a viable route for designing nitrogen fixation catalysts.

One route to increasing reaction rates is the inclusion of transition-metal dopants in TiO_2 [88]. Transition-metal dopants can increase rates via at least two distinct mechanisms: increasing the amount of photo-generated electrons that reach the surface by improving absorption and charge separation, or by altering the kinetics of the surface reaction. Transition-metal doping has been previously explored to improve the performance of TiO_2 photocatalysts [68, 43, 19]. In particular, early work on photocatalytic nitrogen fixation tested a variety of metal dopants. These studies found that several noble metals [61] and iron in particular increase yields [69, 70, 3, 75, 61, 62]. More recently, Hirakawa et al. found that depositing noble metals (Ru, Pt, Pd) onto an already prepared rutile (110) surface led to a decrease in reaction rates [33]. This decrease in rates, along with detailed experimental and theoretical studies on the role of iron dopants [75, 10] suggests that the primary mechanism of these previously-reported dopants is enhanced charge separation. However, transition-metal dopants are also known to affect the surface properties in a range of other materials and reactions [37, 29, 1, 28, 10, 23, 84]. In particular, the field of “single-atom catalysis” has revealed that isolated transition-metal sites supported on oxide materials can exhibit remarkable catalytic properties [44, 60, 58]. However, relatively little effort has been focused on understanding how isolated transition-metal atom dopants affect the surface reactivity of oxides for the conversion of nitrogen to ammonia [76, 45, 89, 7, 42].

In this work, we focus on the potential of isolated transition-metal atoms substituted into the rutile (110) titania surface as a potential route to improve the sur-

face kinetics of the nitrogen reduction reaction. We screen the *d*-block transition-metals substituted onto the (110) surface in two different configurations corresponding to formal oxidation states of 2+ and 4+. We analyze the trends present across the periodic table for the dopant formation energy, N₂, N₂H, and NH₂ adsorption energy. We also map out the thermodynamics of all N₂ reduction pathways and use this to assess the most favorable reaction mechanism. Finally, we assess the expected improvement in reaction rates from forming metal dopant sites on the surface. In this analysis, we consider both electrocatalytic and photocatalytic N₂ reduction. The results illustrate that there are clear correlations in the formation and adsorption energies with the *d*-band center and cohesive energies, respectively. We also find scaling relations between the surface species. These scaling relations result in an optimum in the rate-limiting potential for nitrogen reduction as a function of N₂H and NH₂ adsorption energies.

2 Results and Discussion

Rutile TiO₂ (110) is chosen as a model surface based on the experimentally observed correlation between rutile content and reaction rates for photocatalytic nitrogen fixation [69]. Additionally, there is a rich literature on the surface science of rutile (110) [18, 85, 46, 79], and recent surface-science experiments and DFT calculations indicate that carbon substitution defects on the rutile (110) surface are active for photocatalytic nitrogen reduction [9]. From this model surface, slabs containing metal dopants at the surface in the 2+ and 4+ oxidation states are generated for each dopant metal. In total, all *d*-block transition-metals, except Mn and Cr (23 total), are screened for their surface formation energy and activity for nitrogen reduction. The binding energies of N₂H and NH₂ have been identified as descriptors for activity in the literature as they are typically involved in the rate-limiting steps [34, 53, 10]. Thus, these energies have been calculated to assess the activity of generated surfaces. Full details of the calculation methodology are in the Methods section (Sec. 4).

2.1 Trends In Active Site Formation Energies

The stability of substituted metal surface sites is examined with respect to the position of their *d*-band center. In Fig. 2a, the formation energy of the studied active sites has been plotted against the location of the *d*-band center of the corresponding transition-metal. The pure metallic form is the reference for the formation energy of each metal substituted site. The *d*-band centers are

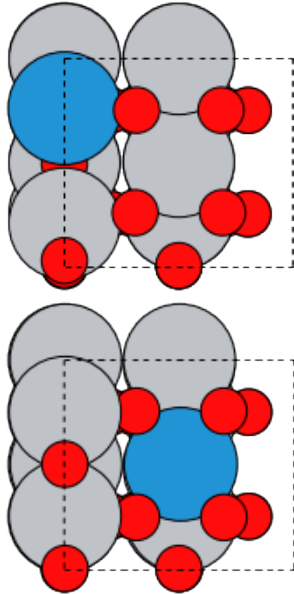


Fig. 1 An example of the screened 2+ (top) and 4+ (bottom) slabs. For 2+ sites the substituent metal has replaced a 6 fold Ti atom (seen in blue) and a bridging oxygen vacancy has been formed to allow the metal to enter the 2+ oxidation state. For 4+ sites the substituent metal has replaced a 5 fold Ti atom (seen in blue) resulting in a 4+ formal oxidation state.

also calculated from the metallic bulk state rather than the single atom. The plot indicates there is a strong correlation between the *d*-band center and formation energy of the metal substitution ($R^2 = 0.89$). We can rationalize the observed correlation in the context of the *d*-band model of chemical bonding [31, 55] summarized in Equation 1 below:

$$\Delta E_d = \int^{E_F} E(\rho'(E) - \rho(E))dE \quad (1)$$

where ΔE_d is the binding energy associated with interaction with the *d*-band, E_F is the Fermi level energy, $\rho(E)$ is the *d*-band density of states before adsorption, and $\rho'(E)$ is the density of states after adsorption. The interaction between adsorbates and the metal's *s*-states are assumed to be approximately constant for all metals, such that variations in binding energies are controlled primarily through bonding interactions with the *d*-band. Interaction with the *d*-band causes the orbitals of the adsorbate to separate into bonding and anti-bonding orbitals. As the *d*-band center approaches the Fermi-level, the anti-bonding orbitals increasingly fill, leading to a weaker bond.

Our system involves a metal atom interacting with an oxide surface rather than an adsorbate binding to the metal surface. We hypothesize that the *d*-orbitals of

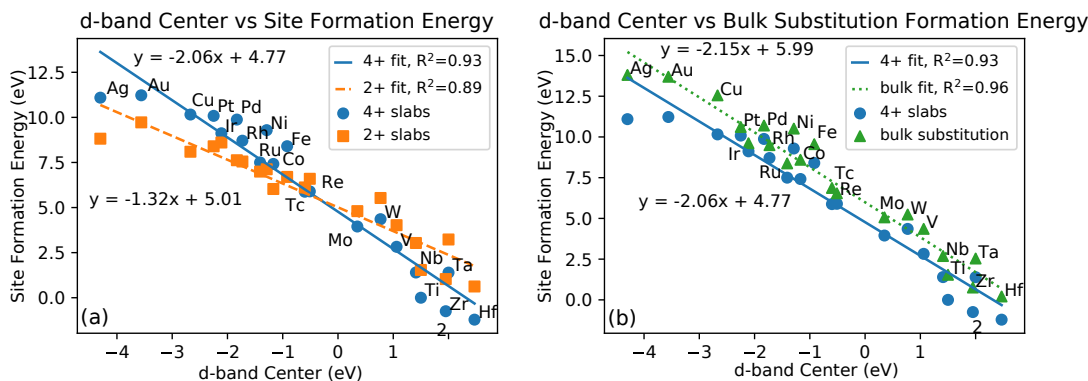


Fig. 2 (a) The formation energy of 4+ surface sites (blue) and 2+ surface sites (orange) with respect to their bulk metallic state vs. the metallic d -band center (b) The formation energy of 4+ surface sites (blue) and bulk substitutions (green) with respect to their bulk metallic state vs. the metallic d -band center. d -band centers were obtained from Ref. 65. Only metals whose d -band center was previously reported in Ref. 65 are included.

the integrated metal atom interact with the p -orbitals of oxygen atoms in the surface similar to the way a metal surface interacts with adsorbing oxygen atoms. This explanation is consistent with the observation that the interaction weakens from left to right on the periodic table, as predicted in the literature [30]. This trend implies that the metals most able to integrate into a surface are those with the most favorable interaction with oxygen. A similar relationship has been reported previously for doped rutile oxides [83] and oxide-supported single-atom catalysts [58]. Other reports suggest that the electronegativity of the substituted metal is the relevant descriptor predicting stability [23]. The electronegativity is also correlated with the formation energy ($R^2=0.78$ and 0.58 for $2+$ and $4+$ respectively, see Fig. S3), but not as strong as the correlation with the d -band center of the metal ($R^2=0.89$ and 0.93 , see Fig. 2). The fact that both of these quantities correlate with the formation energy is not surprising, as a lower energy d -center indicates a more favorable addition of electrons, which is similar to the concept of electronegativity. The main exceptions to this trend are Ti, Zr, Hf, and Ag. The first three can be rationalized easily since all three lie in the same column of the periodic table, which is the same as the host metal, Ti. The improved stability of substituent metals within the group lines up with the chemical intuition since these elements have the same number of valence d electrons. This chemical similarity affords approximately 1.5eV of improved stability relative to the trend. The final outlier, Ag, is more difficult to explain. However, the d -band center of Ag is itself an outlier for its position on the periodic table. This deviation may indicate that more complex bonding in-

teractions are involved that are not easily described by the d -band model.

These results have implications for the relative stability of single-atom sites over surface metal clusters or bulk substitutions in TiO_2 , and will relate to the feasibility of synthesizing metal-doped surfaces experimentally. Some elements (Y, Sc, Zr, Hf) favor integration into the surface structure rather than the formation of surface metal clusters (see Table S1 and S2). Conversely, noble metals such as Rh and Pt do not integrate into the surface favorably and will tend to form surface nano-clusters. This result agrees with TEM measurements in the experimental literature, indicating that clusters of metals such as platinum, silver, gold, nickel, rhodium form on a TiO_2 surface [35, 12, 72, 86] and rutile's reputation as a support [4]. A metal's ability to form surface sites is also dependent on the relative stability of bulk substitution, since a dopant that is more stable in the bulk than the surface will tend to segregate into the bulk rather than forming surface sites. Fig. 2b shows that the 4+ surface sites are more stable than the bulk substitutions for all metals studied. The relative stability of surface sites relative to bulk integration suggests that bulk synthesis techniques such as co-precipitation should lead to a concentration of surface sites that exceeds the concentration of bulk sites for all metals considered. The correlation between the bulk formation energies of dopant metals and their corresponding 4+ surface sites (Fig. 2b) is also striking, indicating that bulk and surface integration are controlled by similar electronic structure interactions.

Fig. 2a also indicates that the oxidation state of the surface site that forms is dependent on the energy of the substituent metal's d -band center. Elements with more

negative d -band centers tend to favor forming 2+ surface sites, whereas more positive d -band centers favor 4+ sites, with the cross-over point being approximately 0.8eV below the fermi-level. This trend makes intuitive sense, as a more negative d -band center implies that the addition of electrons is more favorable, making the more negative oxidation state more stable. For most metals studied the 2+ site is either more stable or nearly as stable, suggesting that the 2+ substitutions are generally more favorable. An alternative interpretation is that the inclusion of metal dopants favors the formation of surface oxygen vacancies, since the 2+ site involves an oxygen vacancy. The reactivity of oxygen vacancies is typically greater than the pristine surface, so promoting oxygen vacancy formation may be yet another indirect mechanism through which metal dopants affect catalytic activity.

2.2 Trends In nitrogen adsorption and cohesive energies

The adsorption of the inert N₂ molecule is required for nitrogen fixation, and the first hydrogenation to N₂H is known to be the potential-limiting step on pure TiO₂ [10]. In addition, the NH₂ → NH₃ reaction has been identified as potential limiting on some materials [34]. This suggests that the trends in N₂, N₂H, and NH₂ binding will provide an indication of a metal’s ability to promote nitrogen reduction. The N₂ and N₂H energies are calculated for both 2+ and 4+ slabs to screen the surface’s ability to reduce N₂. The N₂H binding energy is >1.5eV for all 4+ sites (see Table S2), therefore the subsequent analysis focuses exclusively on 2+ sites.

The results for N₂, N₂H, and NH₂ adsorption on 2+ sites as a function of periodic table group are shown in Fig. 3. The results differ from the typical linear correlation that we expect from the d -band model [55], and instead, show relatively quadratic behavior with a maximum near the middle of the d -block at Os and Re for N₂ and N₂H respectively. Similar results are found for NH₂ adsorption (Fig. 3c), though the magnitude of the adsorption energy varies, and there is small upward trend near the middle of the d -block.

While the N₂, N₂H, and NH₂ binding observed deviates from the near-linear correlation expected from the d -band model, we find a linear correlation between the binding energies and the d -band contributions of the cohesive energies of the corresponding bulk systems (Fig. 4). Cohesive Energy is defined as the change in energy associated with isolated, neutrally charged atoms being brought together to form a bulk material [51]. A metal’s cohesive energy is made up of a d contribution and a s contribution (Eq. 2). Cohesive energies have

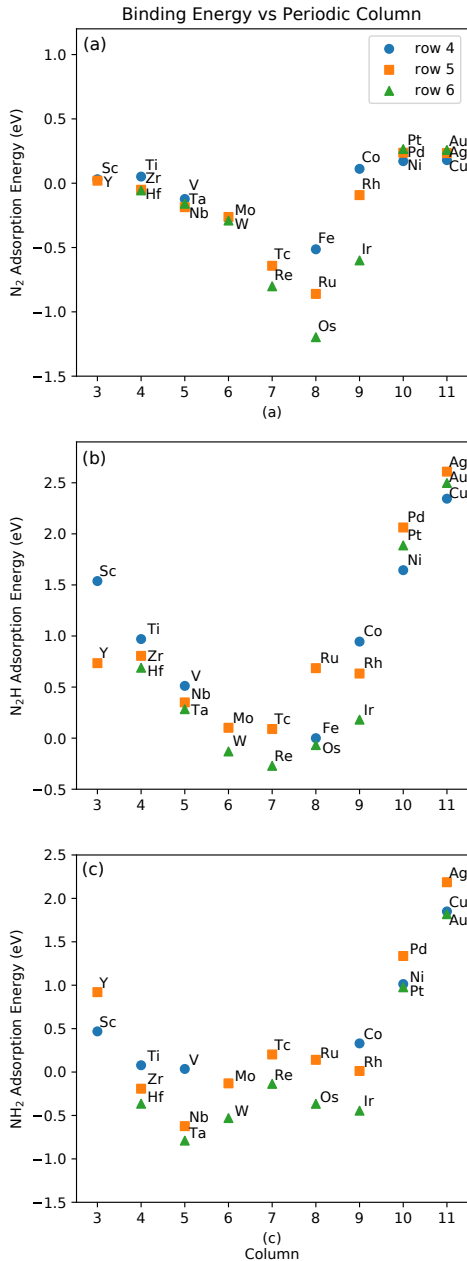


Fig. 3 The binding energies of (a) N₂, (b) N₂H and (c) NH₂ plotted against the periodic column for 2+ metal substituent sites

generally been a measure of the “bulk-nobleness” of a metal [31], with higher cohesive energies correlating to a more noble character. The metals with the highest “bulk-nobleness” are in the center of the d -block and resist corrosion due to the difficulty of breaking their strong metal-metal bonds. In our case, the inverse is true: the stronger the metal-metal bonds of the bulk

material, the stronger the interaction between the metal and a given nitrogen species.

$$E_{coh} = \epsilon_d + \epsilon_s \quad (2)$$

where E_{coh} is the total cohesive energy, ϵ_d is the d contribution and ϵ_s is the s contribution.

The correlation between d -band contribution to cohesive energy and binding is the strongest for N_2H and NH_2 (Fig. 4b-c). These two species show a relatively strong quadratic dependence (Fig. 3b-c) suggesting that the bonding of nitrogen species to these substituent metals is similar to that of forming metal-metal bonds of the original bulk material. Thus, we hypothesize that the physics of nitrogen bonding to these substituent sites is similar to the bonding between single metal atoms and a bulk metal. A similar quadratic trend is seen for N_2 adsorption in Fig. 4a, though there are several outliers near the middle of the d -block (Tc, Ru, Re, Os, Ir) that bind N_2 substantially stronger than predicted by the cohesive energy descriptor. The origin of this anomalously-high reactivity toward N_2 is not clear, though we note that the bonding mechanism changes between physisorption for early/late metals and chemisorption for more reactive metals, indicating that the quadratic trend may still hold for chemisorption.

The trends observed for site formation energy (Fig. 2) and nitrogen compound adsorption energy (Fig. 4) differ qualitatively from trends observed in bulk metals. For single transition-metal dopant atoms, the d -band center controls formation energy, while the cohesive energy controls adsorption energy. In bulk metals the inverse is true: the d -band center controls a material’s ability to bind gas-phase species, whereas the cohesive energy controls how stable the material is [31]. This suggests that the origins of scaling relations for single-atom catalysts or dopant sites may differ from the case of bulk metals. However, we note that the trend does not seem to hold in the case of 4+ sites (see Table S2), and prior work suggests that adsorption energy oxygen is correlated to the d -band center [30], so the trend is not general. The implication of different factors controlling the scaling relations of different adsorbates is that these adsorbates will also not scale with each other. This suggests that single metal atoms or dopants may be able to “break” the scaling relations between adsorbates and reach more active regions of the catalytic phase space [21, 13].

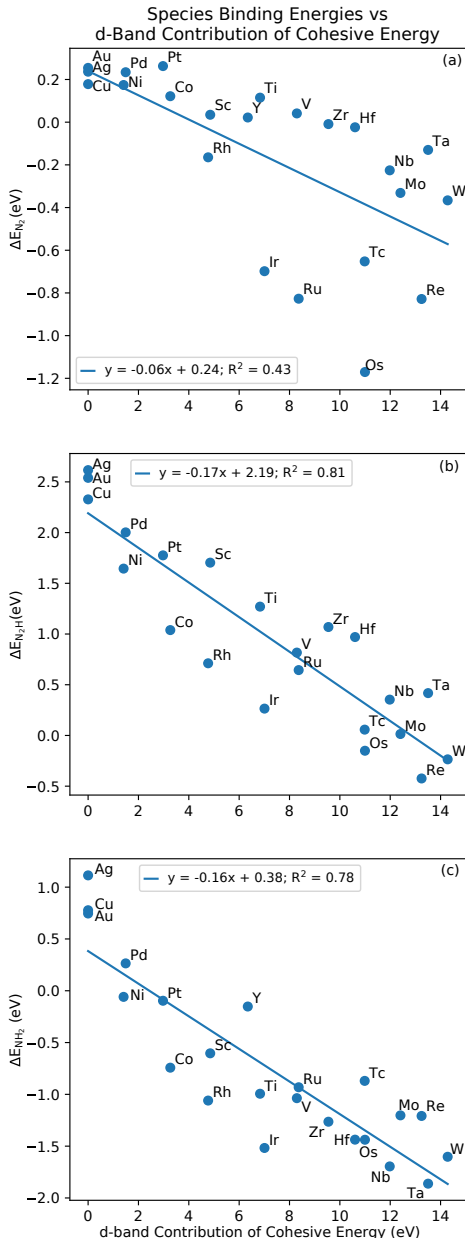


Fig. 4 the d -band contribution to cohesive energies vs. the binding energies of (a) N_2 , (b) N_2H , (c) NH_2 for 2+ metal substituent sites. The d -band cohesive energy contributions obtained from Turchanin and Agraval [77]

2.3 Trends in Catalytic Activity for Nitrogen Reduction

The photocatalytic activity of doped TiO_2 surfaces can be assessed by computing the maximum thermodynamic barrier with electrons at the conduction band edge potential [10], while the electrocatalytic activity of doped

TiO₂ surfaces can be assessed by computing the thermodynamic limiting potential [56, 23]. The computational hydrogen electrode (CHE) provides a route to computing the thermochemical potential of electrons at the TiO₂ surface (Sec. 4.3), and the resulting analysis provides only a thermodynamic picture of the reaction pathway. This analysis establishes a lower bound on the kinetics and correlates well with experimental trends in the literature [71].

Computing the maximum barrier or limiting potential requires the free energies of each state along a given reaction pathway. The full thermodynamics of the N₂ reduction reaction pathways on all 2+ sites were calculated, allowing the generation of free energy diagrams for all possible reaction pathways (Fig. S4-S109, Table S1). Höskuldsson et al. [34] also previously found strong scaling relations between the binding of nitrogen compounds and the N₂H binding energy for rutile metal oxides. The binding energies of all species are fit to linear scaling relations with N₂H and NH₂ as descriptors to assess the scaling relations for this system (Fig. S1). The scaling relations have a root mean squared error on the order of 0.2 eV, consistent with general scaling relations for other reactions [81]. The N₂H and NH₂ were also used to fit scaling relationships for all electrochemical steps, yielding similar accuracy to scaling relations for individual species (Fig. S2). These scaling relations directly predicting reaction energies are used for subsequent analyses.

The electrochemical limiting potential is calculated for all surfaces to assess their ability to reduce N₂ under applied bias. The results are plotted against the NH₂ binding energy in Fig. 5a. This plot reveals a clear volcano relationship between the NH₂ binding energy and the limiting potential. Free energy diagrams have been generated for selected elements and can be seen in Fig. 6. In contrast to prior work by Höskuldsson et al. [34] and Montoya et al. [53], we find that the NH₂ binding energy is a slightly more reliable descriptor than N₂H binding; however these quantities are linked by scaling relations, indicating that either descriptor will provide consistent trends. In this case, the limiting step shifts from NH₂ desorption on the left to N₂ hydrogenation on the right, with most dopants being limited by NH₂ desorption. This means that NH₂ adsorption energy directly controls the reactive side of the volcano, and explains why it is an accurate descriptor in this case.

To better understand the relationship between the descriptors, limiting potential, and limiting steps, the fits of the scaling relations (see Fig. S2) were used to generate a two dimensional volcano plot (Fig. 5b). As with the scaling relations, the root mean squared error of the predicted limiting potential in Fig. 5b is roughly

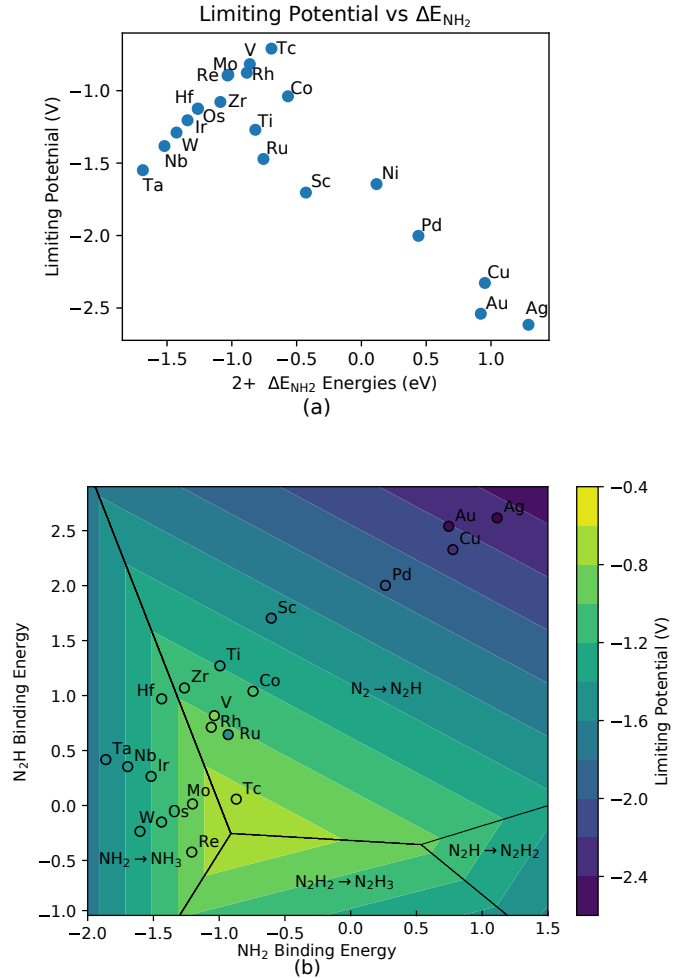


Fig. 5 (a) The limiting potential vs the NH₂ binding energy. The data for this plot can be seen in Table S3 (b) A two dimensional volcano plot for electrochemical limiting potential using N₂H and NH₂ as descriptors for the studied systems. Points are colored in with the limiting potential calculated from DFT. Any surface for which a full path was not available has been excluded.

0.2V. The results confirm the findings from Fig. 5a, but provide additional insight into the limiting steps. The deviation from the NH₂/N₂H scaling for reactive dopants (NH₂ binding < -0.75 eV) leads to a cluster of dopants that behave similarly for different reasons. For example, the limiting potential and NH₂ adsorption for Mo and V are nearly identical, but the mechanism shifts between the two with V being limited by N₂H formation and Mo being limited by NH₂ desorption. The results also show that the optimal limiting potential is still relatively large (~-0.4 V), and that Tc is near-optimal.

Overall, the results suggest that several dopants are capable of improving the performance over pure TiO₂. The elements that show significant improvement are Tc,

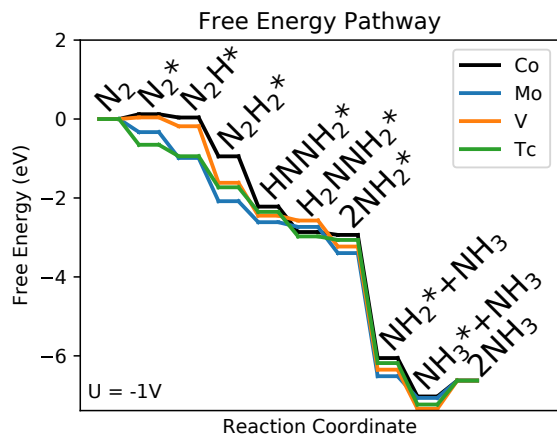


Fig. 6 A free energy diagram at -1V relative to RHE for the most promising elements: Co, Mo, V, and Tc.

Co, Mo, V, Rh, and Re. Tc sits at the top of the volcano. The high activity of Tc presents a serious problem for experimental testing or practical application since Tc is a scarce, synthetically produced element. Further complicating matters, most isotopes of Tc are radioactive. In addition, the active sites may be challenging to synthesize due to their relatively high formation energy (Fig. 2). On the other hand, the relatively low limiting potential of Co, Mo, V, Rh, and Re are promising results. Co, Mo, and V are relatively inexpensive and abundant, whereas Re and Rh are relatively scarce [78]. These elements are promising dopants for improving catalytic rates on TiO_2 . However, synthesis may be a challenge since the formation energy of the surface sites is generally positive relative to the bulk metals (Fig. 2). Nonetheless, the results indicate that Co is the most promising dopant for reducing the thermodynamic limiting potential of ammonia synthesis on TiO_2 .

A second consideration when assessing the electrocatalytic activity of a surface is the largest thermochemical barrier. Thermochemical steps do not involve electron transfers, so they are not considered when computing the limiting potential. However, they may still present a substantial barrier that will affect the overall rate. The largest thermochemical barriers for each surface can be seen in Table S4. The three steps with significant thermochemical barriers are N_2 adsorption, $\text{NH}_2\text{-NH}_2$ scission, and NH_3 desorption. For the case of the most promising dopant, Co, the adsorption of N_2 is endergonic by 0.12 eV, which may lead to low N_2^* coverages under competitive adsorption with H_2O . Moreover, there is a substantial thermochemical barrier of 0.43 eV for NH_3 desorption. Desorption of NH_3 is the thermochemical limiting step for most dopants,

suggesting that NH_3 may exist at high coverages or even poison the surface. However, solvation effects have been neglected, and the free energy is computed at a chemical potential of NH_3 equivalent to 1 bar, suggesting that NH_3 desorption may not be limiting in aqueous solutions with low NH_3 concentrations. Some of the noble dopants (Pd, Ag, Au, and Cu) also show substantial thermochemical barriers of 0.5-1.5 eV for $\text{NH}_2\text{-NH}_2$ scission, indicating that rates for these metals will be low even at the limiting potential. A more detailed kinetic analysis of both electrochemical and thermochemical activation energies is required to predict the electrocatalytic rate for any dopant, but this thermochemical analysis provides lower bound for the kinetic barrier.

Finally, we assess the ability of dopant metals to improve photocatalytic nitrogen reduction. This is calculated based on the largest thermodynamic barrier at a reductive potential equal to the conduction band edge of TiO_2 (approximately -0.15 V vs. RHE [57]). This approach assumes that the conduction band edge of TiO_2 is not significantly affected by the presence of the dopant, and neglects improvements in other bulk photochemical properties such as charge separation or carrier lifetime. Nonetheless, it provides a good starting point for assessing the impact of dopant metals on the surface catalytic properties. The highest thermodynamic barrier for the best reaction pathway is plotted vs. the NH_2^* binding energy in Fig. 7. The results are qualitatively similar to the electrochemical limiting potentials in Fig. 5, but there are some deviations that occur for two reasons. The first is that the photochemical analysis includes both thermochemical and electrochemical steps. The desorption of NH_3^* is a thermochemical step that becomes rate-limiting for reactive surfaces. For less reactive surfaces the electrochemical step of N_2 hydrogenation is rate-limiting, which becomes slightly more favorable under the applied bias, effectively shifting the right side of the volcano downward. The second reason for deviation is that multi-electron transfers are less sensitive to small potentials, so dopants such as Tc which have relatively unstable $\text{N}_2\text{H}_{x>2}$ states are not as favorable under photocatalytic conditions. Overall, the results suggest that the minimum thermodynamic barriers of 0.93 eV, 0.90 eV, 0.89 eV, 0.73 eV, for Zr, Co, Mo, and Rh, respectively. This represents a substantial improvement over the 1.21 eV limiting potential for pure Ti, indicating that these metals may act as surface promoters for photocatalytic nitrogen reduction if kinetic barriers are low.

Experimental observations can provide further insight into the computational predictions. Several prior reports have investigated transition-metal dopants for

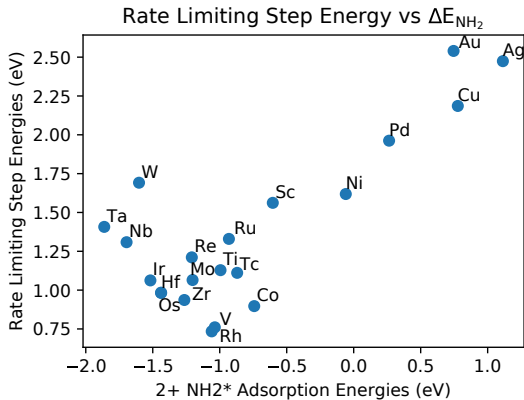


Fig. 7 The highest barrier observed vs the NH₂ binding energy with the potential set to band edge of rutile. The data for this plot can be seen in Table S5. Any surface for which a full path was not available has been excluded.

enhancing photocatalytic ammonia production on TiO₂ [69, 61, 33]. Interestingly Schrauzer et al. reports increases in ammonia yield in the presence of Co and Mo dopants [69], though this report comes from the early literature and rigorous controls [26] or isotopic labeling studies [2] were not included. Moreover, the same report revealed enhanced rates for Fe and Ni, so the confirmation of the prediction regarding the former two should be treated with caution. The rate enhancement for noble metals such as Ru, Rh, and Pd is conflicting even in the early literature, with Schrauzer and Guth reporting no enhancement [69]. However, Ranjit et al. reported enhancement for all noble metals with the most significant improvement for Ru [61]. In all of these systems, the metal dopants were incorporated via co-precipitation, and catalysts were polycrystalline TiO₂, indicating that the metals may also enhance yields via charge separation, mediation of crystallization, or other mechanisms [49]. Hirakawa et al. added Ru, Pt, and Pd to pre-synthesized TiO₂ particles and reported no significant improvement in the reaction rates [33]. These experiments are more consistent with the computational model system used in this study since only surface properties are affected, and the results are consistent with the prediction that these noble metals will not affect the rate. However, further systematic and well-controlled experiments that characterize the state of the metal incorporation in the TiO₂ surface are required to validate the predicted trends.

3 Conclusions

The stability of metal dopant surface sites and their effects on the reaction thermodynamics of N₂ reduction

on rutile (110) are studied using DFT. We find that the formation energy of these doped surface states is strongly related to the location of the *d*-band center of the substituted metal, with a trend consistent with the *d*-band model. We also find a correlation between the cohesive energy of metals and their N₂H and NH₂ binding energy on the surface, suggesting that the bonding of nitrogen species is similar to that of bulk metals. Finally, we investigate the effects of dopant sites on the full reaction pathways for 2+ sites on all studied metals. We find a clear volcano relationship between NH₂ binding and both the electrochemical limiting potential and the highest thermodynamic barrier for photocatalytic reactions. The formation of Co and Mo 2+ sites is proposed to yield a slight improvement of reaction rates in both electrocatalysis and photocatalysis. Other metals commonly used in catalysis, such as Ir, and Pd are predicted to have a limited or detrimental effect on the surface catalytic properties of TiO₂ for nitrogen reduction. This suggests that the role of metal dopants in photocatalytic ammonia synthesis by TiO₂ is likely related to modifications of bulk properties in most cases. However, the existence of clear trends in the formation energy and reactivity of single metal atom dopants toward nitrogen intermediates suggests that computational design of metal-doped oxide materials is a promising strategy for other oxide systems and/or other nitrogen conversion reactions.

4 Methods

4.1 Density Functional Theory Calculations

All first principles calculations are performed in the Quantum Espresso software package [25]. The TiO₂ slabs and atomistic images are created using the Atomic Simulation Environment (ASE) package [39]. Spin polarization is used in all simulations to ensure the lowest energy spin state is obtained for each site. The BEEF-vdW functional [82] is used with plane wave cutoff of 400 eV and a Monkhorst-Pack k-point grid spacing of 4×4×1 [52]. The efficiency versions of the standard solid state pseudopotentials [24] (SSSP) are used for all calculations because of their high reported accuracy [40]. The convergence threshold is set at 10⁻⁶ eV and Fermi-Dirac smearing of 0.1 eV is used. All structures are converged to a maximum force smaller than 0.05 eV/Å using the BFGS line search algorithm. Adsorption energies are obtained from the DFT calculations by subtracting the energy of a clean slab and the energy of the free gas molecule from the energy of the gas adsorbed

to the slab:

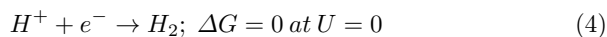
$$E_{\text{adsorption}} = E_{\text{slab+adsorbate}} - E_{\text{slab}} - E_{\text{adsorbate}} \quad (3)$$

4.2 Thermochemistry

To calculate the adsorption energy at standard temperature and pressure, the thermochemistry package from ASE is used [39]. The contributions of zero point energy (ZPE) have been included for all systems. Free gasses are approximated in the ideal gas limit, and adsorbed gasses in the harmonic limit [63]. A frequency cutoff of 33 cm^{-1} for low frequency modes was selected. The vibrational mode for all metals were assumed to be approximately the same as those of the respective species adsorbed to the oxygen vacant TiO_2 (110) surface, thus the same thermodynamic correction values are applied to all species of the same type.

4.3 Photochemistry

The photochemistry has been treated using the methods outlined by Hellman et. al. [32]. Within this framework, the effects of excited states are neglected allowing the treatment of excited electrons and holes using the computational hydrogen electrode model (CHE). In this formalism, the reference electrode is set by setting the free energy of hydrogen evolution reaction (HER) to zero:



The potentials of electrons and holes are set at the value of the band edges of the rutile [57].

4.4 Model Surface Generation

The surfaces are constructed with 4 TiO_2 tri-layers (bottom 2 layers constrained to bulk positions), with a 1×2 supercell repeat. The pristine slab totals 48 atoms, with 4 Ti and 8 O per tri-layer. 6 Å of vacuum are added on both top and bottom of the slab and a dipole correction is applied in the z direction [5]. The lattice parameters of the unit cells are fixed at the calculated value for pure rutile TiO_2 . 2+ sites were created by replacing the six-fold titanium site with the substituent metal and removing a single bridging oxygen (see Fig. 1) 4+ sites were generated by replacing the five-fold titanium site with the substituent metal. The adsorption site was selected to directly over the substituent metals.

5 Acknowledgements

We would like to thank Fuhzu Liu and Gabriel Gusmão for their comments and suggestions for improving this manuscript. This material is based upon work supported by the U. S. Department of Energy, Office of Science, Office of Basic Energy Sciences Computational Chemical Sciences program under Award No.de-sc0019410.

References

1. S. C. Ammal and A. Heyden. Water-gas shift activity of atomically dispersed cationic platinum versus metallic platinum clusters on titania supports. *ACS Catalysis*, 7(1):301–309, dec 2016.
2. S. Z. Andersen, V. Čolić, S. Yang, J. A. Schwalbe, A. C. Nielander, J. M. McEnaney, K. Enemark-Rasmussen, J. G. Baker, A. R. Singh, B. A. Rohr, M. J. Statt, S. J. Blair, S. Mezzavilla, J. Kibsgaard, P. C. K. Vesborg, M. Cargnello, S. F. Bent, T. F. Jaramillo, I. E. L. Stephens, J. K. Nørskov, and I. Chorkendorff. A rigorous electrochemical ammonia synthesis protocol with quantitative isotope measurements. *Nature*, 570(7762):504–508, may 2019.
3. V. Augugliaro, A. Lauricella, L. Rizzuti, M. Schiavello, and A. Sclafani. Conversion of solar energy to chemical energy by photoassisted processes—I. Preliminary results on ammonia production over doped titanium dioxide catalysts in a fluidized bed reactor. *Int. J. Hydrogen Energy*, 7(11):845–849, 1982.
4. S. Bagheri, N. M. Julkapli, and S. B. A. Hamid. Titanium dioxide as a catalyst support in heterogeneous catalysis. *The Scientific World Journal*, 2014:1–21, 2014.
5. L. Bengtsson. Dipole correction for surface supercell calculations. *Phys. Rev. B*, 59:12301–12304, May 1999.
6. R. I. Bickley and V. Vishwanathan. Photocatalytically induced fixation of molecular nitrogen by near UV radiation. *Nature*, 280(5720):306–308, jul 1979.
7. S. Cheng, Y.-J. Gao, Y.-L. Yan, X. Gao, S.-H. Zhang, G.-L. Zhuang, S.-W. Deng, Z.-Z. Wei, X. Zhong, and J.-G. Wang. Oxygen vacancy enhancing mechanism of nitrogen reduction reaction property in Ru/TiO_2 . *Journal of Energy Chemistry*, 39:144–151, dec 2019.
8. B. M. Comer, P. Fuentes, C. O. Dimkpa, Y.-H. Liu, C. A. Fernandez, P. Arora, M. Realf, U. Singh, M. C. Hatzell, and A. J. Medford. Prospects and challenges for solar fertilizers. *Joule*, 3(7):1578–1605, jul 2019.

9. B. M. Comer, Y.-H. Liu, M. B. Dixit, K. B. Hatzell, Y. Ye, E. J. Crumlin, M. C. Hatzell, and A. J. Medford. The role of adventitious carbon in photocatalytic nitrogen fixation by titania. *Journal of the American Chemical Society*, 140(45):15157–15160, 2018.
10. B. M. Comer and A. J. Medford. Analysis of photocatalytic nitrogen fixation on rutile TiO₂(110). *ACS Sustainable Chemistry & Engineering*, 6(4):4648–4660, feb 2018.
11. X. Cui, C. Tang, and Q. Zhang. A Review of Electrocatalytic Reduction of Dinitrogen to Ammonia under Ambient Conditions. *Advanced Energy Materials*, 8(22):1–25, 2018.
12. T. M. D. Dang, T. M. H. Nguyen, and H. P. Nguyen. The preparation of nano-gold catalyst supported on iron doped titanium oxide. *Advances in Natural Sciences: Nanoscience and Nanotechnology*, 1(2):025011, jun 2010.
13. M. T. Darby, M. Stamatakis, A. Michaelides, and E. C. H. Sykes. Lonely atoms with special gifts: Breaking linear scaling relationships in heterogeneous catalysis with single-atom alloys. *The Journal of Physical Chemistry Letters*, 9(18):5636–5646, sep 2018.
14. J. A. Davies, D. L. Boucher, and J. G. Edwards. The question of artificial photosynthesis of ammonia on heterogeneous catalysts. In *Advances in Photochemistry*, pages 235–310. John Wiley & Sons, Inc., 1995.
15. J. A. Davies and J. G. Edwards. Reply: Standards of Demonstration for the Heterogeneous Photoreactions of N₂ with H₂O. *Angew. Chem. Int. Ed.*, 32(4):552–553, 1993.
16. F. J. de Bruijn. The quest for biological nitrogen fixation in cereals: A perspective and prospective. In *Biological Nitrogen Fixation*, pages 1087–1101. John Wiley & Sons, Inc, jul 2015.
17. N. Dhar, E. Seshacharyulu, and N. Biswas. New aspects of nitrogen fixation and loss in soils. *Proceedings of the National institute of sciences of India*, 7:115–131, 1941.
18. U. Diebold. The surface science of titanium dioxide. *Surface Science Reports*, 48(5-8):53–229, jan 2003.
19. M. V. Dozzi and E. Selli. Doping TiO₂ with p-block elements: Effects on photocatalytic activity. *Journal of Photochemistry and Photobiology C: Photochemistry Reviews*, 14:13–28, mar 2013.
20. J. G. Edwards, J. A. Davies, D. L. Boucher, and A. Mennad. An Opinion on the Heterogeneous Photoreactions of N₂ with H₂O. *Angew. Chem. Int. Ed.*, 31(4):480–482, 1992.
21. T. Z. H. Gani and H. J. Kulik. Understanding and breaking scaling relations in single-site catalysis: Methane to methanol conversion by Fe^{IV}=O. *ACS Catalysis*, 8(2):975–986, jan 2018.
22. X. Gao, Y. Wen, D. Qu, L. An, S. Luan, W. Jiang, X. Zong, X. Liu, and Z. Sun. Interference effect of alcohol on nessler’s reagent in photocatalytic nitrogen fixation. *ACS Sustainable Chemistry & Engineering*, 6(4):5342–5348, mar 2018.
23. M. García-Mota, A. Vojvodic, H. Metiu, I. C. Man, H.-Y. Su, J. Rossmeisl, and J. K. Nørskov. Tailoring the activity for oxygen evolution electrocatalysis on rutile TiO₂(110) by transition-metal substitution. *ChemCatChem*, 3(10):1607–1611, aug 2011.
24. I. E. C. N. M. N. M. Gianluca Prandini, Antimo Marrazzo. A standard solid state pseudopotentials (sssp) library optimized for accuracy and efficiency (version 1.0, data download), 2018.
25. P. Giannozzi, S. Baroni, N. Bonini, M. Calandra, R. Car, C. Cavazzoni, D. Ceresoli, G. L. Chiarotti, M. Cococcioni, I. Dabo, A. Dal Corso, S. de Gironcoli, S. Fabris, G. Fratesi, R. Gebauer, U. Gerstmann, C. Gougoussis, A. Kokalj, M. Lazzeri, L. Martin-Samos, N. Marzari, F. Mauri, R. Mazzarello, S. Paolini, A. Pasquarello, L. Paulatto, C. Sbraccia, S. Scandolo, G. Sclauzero, A. P. Seitsonen, A. Smogunov, P. Umari, and R. M. Wentzcovitch. Quantum espresso: a modular and open-source software project for quantum simulations of materials. *Journal of Physics: Condensed Matter*, 21(39):395502 (19pp), 2009.
26. L. F. Greenlee, J. N. Renner, and S. L. Foster. The use of controls for consistent and accurate measurements of electrocatalytic ammonia synthesis from dinitrogen. *ACS Catalysis*, 8(9):7820–7827, jul 2018.
27. M. Gross. We need to talk about nitrogen. *Current Biology*, 22, 2012.
28. X.-K. Gu, C.-Q. Huang, and W.-X. Li. First-principles study of single transition metal atoms on ZnO for the water gas shift reaction. *Catalysis Science & Technology*, 7(19):4294–4301, 2017.
29. X.-K. Gu, B. Qiao, C.-Q. Huang, W.-C. Ding, K. Sun, E. Zhan, T. Zhang, J. Liu, and W.-X. Li. Supported single pt1/au1 atoms for methanol steam reforming. *ACS Catalysis*, 4(11):3886–3890, oct 2014.
30. B. Hammer and J. Nørskov. Theoretical surface science and catalysis—calculations and concepts. In *Advances in Catalysis*, pages 71–129. Elsevier, 2000.
31. B. Hammer and J. K. Nørskov. Why gold is the noblest of all the metals. *Nature*, 376(6537):238–

- 240, jul 1995.
32. A. Hellman and B. Wang. First-Principles View on Photoelectrochemistry: Water-Splitting as Case Study. *Inorganics*, 5(2):37, 2017.
 33. H. Hirakawa, M. Hashimoto, Y. Shiraishi, and T. Hirai. Photocatalytic conversion of nitrogen to ammonia with water on surface oxygen vacancies of titanium dioxide. *Journal of the American Chemical Society*, 139(31):10929–10936, jul 2017.
 34. Á. B. Höskuldsson, Y. Abghoui, A. B. Gunnarsdóttir, and E. Skúlason. Computational screening of rutile oxides for electrochemical ammonia formation. *ACS Sustainable Chemistry & Engineering*, 5(11):10327–10333, sep 2017.
 35. V. Iliev, D. Tomova, L. Bilyarska, A. Eliyas, and L. Petrov. Photocatalytic properties of TiO₂ modified with platinum and silver nanoparticles in the degradation of oxalic acid in aqueous solution. *Applied Catalysis B: Environmental*, 63(3-4):266–271, mar 2006.
 36. J. Jia, L. C. Seitz, J. D. Benck, Y. Huo, Y. Chen, J. W. D. Ng, T. Bilir, J. S. Harris, and T. F. Jaramillo. Solar water splitting by photovoltaic-electrolysis with a solar-to-hydrogen efficiency over 30%. *Nature Communications*, 7(1), oct 2016.
 37. M. E. Khan, M. M. Khan, and M. H. Cho. Recent progress of metal-graphene nanostructures in photocatalysis. *Nanoscale*, 10(20):9427–9440, 2018.
 38. V. Kyriakou, I. Garagounis, E. Vasileiou, A. Vourros, and M. Stoukides. Progress in the electrochemical synthesis of ammonia. *Catalysis Today*, 286:2–13, may 2017.
 39. A. H. Larsen, J. J. Mortensen, J. Blomqvist, I. E. Castelli, R. Christensen, M. Duak, J. Friis, M. N. Groves, B. Hammer, C. Hargus, E. D. Hermes, P. C. Jennings, P. B. Jensen, J. Kermode, J. R. Kitchin, E. L. Kolsbjerg, J. Kubal, K. Kaasbjerg, S. Lysgaard, J. B. Maronsson, T. Maxson, T. Olsen, L. Pastewka, A. Peterson, C. Rostgaard, J. Schitz, O. Schtt, M. Strange, K. S. Thygesen, T. Vegge, L. Vilhelmsen, M. Walter, Z. Zeng, and K. W. Jacobsen. The atomic simulation environmenta python library for working with atoms. *Journal of Physics: Condensed Matter*, 29(27):273002, 2017.
 40. K. Lejaeghere, G. Bihlmayer, T. Björkman, P. Blaha, S. Blügel, V. Blum, D. Caliste, I. E. Castelli, S. J. Clark, A. Dal Corso, S. de Gironcoli, T. Deutsch, J. K. Dewhurst, I. Di Marco, C. Draxl, M. Dulak, O. Eriksson, J. A. Flores-Livas, K. F. Garrity, L. Genovese, P. Giannozzi, M. Giantomassi, S. Goedecker, X. Gonze, O. Grånäs, E. K. U. Gross, A. Gulans, F. Gygi, D. R. Hamann, P. J. Hasnip, N. A. W. Holzwarth, D. Iuşan, D. B. Jochym, F. Jollet, D. Jones, G. Kresse, K. Koepnik, E. Küçükbenli, Y. O. Kvashnin, I. L. M. Locht, S. Lubeck, M. Marsman, N. Marzari, U. Nitzsche, L. Nordström, T. Ozaki, L. Paulatto, C. J. Pickard, W. Poelmans, M. I. J. Probert, K. Refson, M. Richter, G.-M. Rignanese, S. Saha, M. Scheffler, M. Schlipf, K. Schwarz, S. Sharma, F. Tavazza, P. Thunström, A. Tkatchenko, M. Torrent, D. Vanderbilt, M. J. van Setten, V. Van Speybroeck, J. M. Wills, J. R. Yates, G.-X. Zhang, and S. Cottenier. Reproducibility in density functional theory calculations of solids. *Science*, 351(6280), 2016.
 41. C. Li, T. Wang, Z.-J. Zhao, W. Yang, J.-F. Li, A. Li, Z. Yang, G. A. Ozin, and J. Gong. Promoted fixation of molecular nitrogen with surface oxygen vacancies on plasmon-enhanced TiO₂ photoelectrodes. *Angewandte Chemie International Edition*, 57(19):5278–5282, mar 2018.
 42. S.-J. Li, D. Bao, M.-M. Shi, B.-R. Wulan, J.-M. Yan, and Q. Jiang. Amorphizing of au nanoparticles by CeO_x-RGO hybrid support towards highly efficient electrocatalyst for n₂reduction under ambient conditions. *Advanced Materials*, 29(33):1700001, jul 2017.
 43. Y. Li, S. Peng, F. Jiang, G. Lu, and S. Li. Effect of doping TiO₂ with alkaline-earth metal ions on its photocatalytic activity. *Journal of the Serbian Chemical Society*, 72(4):393–402, 2007.
 44. J. Liu. Catalysis by supported single metal atoms. *ACS Catalysis*, 7(1):34–59, nov 2016.
 45. S. Liu, Y. Wang, S. Wang, M. You, S. Hong, T.-S. Wu, Y.-L. Soo, Z. Zhao, G. Jiang, J. Qiu, B. Wang, and Z. Sun. Photocatalytic fixation of nitrogen to ammonia by single Ru atom decorated TiO₂ nanosheets. *ACS Sustainable Chemistry & Engineering*, 7(7):6813–6820, feb 2019.
 46. G. Lu, a. Linsebigler, and J. T. Yates. Ti3+ Defect Sites on TiO₂(110): Production and Chemical Detection of Active Sites. *Journal of Physical Chemistry*, 98(45):11733–11738, 1994.
 47. J. W. McArthur and G. C. McCord. Fertilizing growth: Agricultural inputs and their effects in economic development. *Journal of Development Economics*, 127:133–152, jul 2017.
 48. I. J. McPherson, T. Sudmeier, J. Fellowes, and S. C. E. Tsang. Materials for electrochemical ammonia synthesis. *Dalton Transactions*, 48(5):1562–1568, 2019.
 49. A. J. Medford and M. C. Hatzell. Photon-driven nitrogen fixation: Current progress, thermodynamic considerations, and future outlook. *ACS Catalysis*, pages 2624–2643, mar 2017.

50. R. Michalsky, A. M. Avram, B. A. Peterson, P. H. Pfromm, and A. A. Peterson. Chemical looping of metal nitride catalysts: low-pressure ammonia synthesis for energy storage. *Chem. Sci.*, 6:3965–3974, 2015.
51. U. Mizutani, M. Inukai, H. Sato, and E. Zijlstra. 2-electron theory of complex metallic alloys. In D. E. Laughlin and K. Hono, editors, *Physical Metallurgy (Fifth Edition)*, pages 103 – 202. Elsevier, Oxford, fifth edition edition, 2014.
52. H. J. Monkhorst and J. D. Pack. Special points for brillouin-zone integrations. *Physical Review B*, 13(12):5188–5192, jun 1976.
53. J. H. Montoya, C. Tsai, A. Vojvodic, and J. K. Nørskov. The challenge of electrochemical ammonia synthesis: A new perspective on the role of nitrogen scaling relations. *ChemSusChem*, 8(13):2180–2186, 2015.
54. A. Nakamura, Y. Ota, K. Koike, Y. Hidaka, K. Nishioka, M. Sugiyama, and K. Fujii. A 24.4% solar to hydrogen energy conversion efficiency by combining concentrator photovoltaic modules and electrochemical cells. *Applied Physics Express*, 8(10):107101, 2015.
55. A. Nilsson and L. G. Pettersson. Adsorbate electronic structure and bonding on metal surfaces. In *Chemical Bonding at Surfaces and Interfaces*, pages 57–142. Elsevier, 2008.
56. J. K. Nørskov, J. Rossmeisl, A. Logadottir, L. Lindqvist, J. R. Kitchin, T. Bligaard, and H. Jónsson. Origin of the overpotential for oxygen reduction at a fuel-cell cathode. *J. Phys. Chem. B*, 108(46):17886–17892, nov 2004.
57. A. J. Nozik and R. Memming. Physical chemistry of semiconductor-liquid interfaces. *The Journal of Physical Chemistry*, 100(31):13061–13078, jan 1996.
58. N. J. O’Connor, A. S. M. Jonayat, M. J. Janik, and T. P. Senftle. Interaction trends between single metal atoms and oxide supports identified with density functional theory and statistical learning. *Nature Catalysis*, 1(7):531–539, jul 2018.
59. P.A. Fuentes, B. Bumb, and M. Johnson. Improving fertilizer markets in west africa: The fertilizer supply chain in senegal. Technical report, International Fertilizer Development Center and International Food Policy Research Institute, Muscle Shoals, Alabama, December 2012.
60. B. Qiao, A. Wang, X. Yang, L. F. Allard, Z. Jiang, Y. Cui, J. Liu, J. Li, and T. Zhang. Single-atom catalysis of CO oxidation using pt1/FeOx. *Nature Chemistry*, 3(8):634–641, jul 2011.
61. K. Ranjit, T. Varadarajan, and B. Viswanathan. Photocatalytic reduction of dinitrogen to ammonia over noble-metal-loaded TiO₂. *Journal of Photochemistry and Photobiology A: Chemistry*, 96(1-3):181–185, may 1996.
62. K. Ranjit and B. Viswanathan. Photocatalytic reduction of nitrite and nitrate ions to ammonia on m/TiO₂ catalysts. *Journal of Photochemistry and Photobiology A: Chemistry*, 108(1):73–78, jul 1997.
63. K. Reuter, C. Stampf, and M. Scheffler. AB initio atomistic thermodynamics and statistical mechanics of surface properties and functions. In *Handbook of Materials Modeling*, pages 149–194. Springer Nature, 2005.
64. S. K. Ritter. The haber-bosch reaction: An early chemical impact on sustainability. *C&EN*, 86, 2018.
65. A. Ruban, B. Hammer, P. Stoltze, H. Skriver, and J. Nørskov. Surface electronic structure and reactivity of transition and noble metals1communication presented at the first francqui colloquium, brussels, 19–20 february 1996.1. *Journal of Molecular Catalysis A: Chemical*, 115(3):421–429, feb 1997.
66. Z. J. Schiffer and K. Manthiram. Electrification and decarbonization of the chemical industry. *Joule*, 1(1):10–14, Sep 2017.
67. R. Schlögl. Catalytic synthesis of ammonia - a “never-ending story”? *Angewandte Chemie International Edition*, 42(18):2004–2008, may 2003.
68. J. Schneider, M. Matsuoka, M. Takeuchi, J. Zhang, Y. Horiuchi, M. Anpo, and D. W. Bahnemann. Understanding TiO₂ photocatalysis: Mechanisms and materials. *Chemical Reviews*, 114(19):9919–9986, 2014. PMID: 25234429.
69. G. Schrauzer and T. Guth. Photocatalytic reactions. 1. Photolysis of water and photoreduction of nitrogen on titanium dioxide. *J. Am. Chem. Soc.*, 99(22):7189–7193, 1977.
70. G. N. Schrauzer, N. Strampach, L. N. Hui, M. R. Palmer, and J. Salehi. Nitrogen photoreduction on desert sands under sterile conditions. *Proc. Natl. Acad. Sci. U.S.A.*, 80(12):3873–3876, 1983.
71. Z. W. Seh, J. Kibsgaard, C. F. Dickens, I. Chorkendorff, J. K. Nørskov, and T. F. Jaramillo. Combining theory and experiment in electrocatalysis: Insights into materials design. *Science*, 355(6321), 2017.
72. V. M. Shinde and G. Madras. CO methanation toward the production of synthetic natural gas over highly active Ni/TiO₂catalyst. *AIChE Journal*, 60(3):1027–1035, nov 2013.
73. A. R. Singh, B. A. Rohr, J. A. Schwalbe, M. Cargnello, K. Chan, T. F. Jaramillo, I. Chork-

- endorff, and J. K. Nørskov. Electrochemical ammonia synthesis-the selectivity challenge. *ACS Catal.*, 7(1):706–709, jan 2017.
74. V. Smil. Detonator of the population explosion. *Nature*, 400(6743):415–415, jul 1999.
75. J. Soria, J. C. Conesa, V. Augugliaro, L. Palmisano, M. Schiavello, and A. Sclafani. Dinitrogen photoreduction to ammonia over titanium dioxide powders doped with ferric ions. *J. Phys. Chem.*, 95(1):274–282, jan 1991.
76. H. Tao, C. Choi, L.-X. Ding, Z. Jiang, Z. Han, M. Jia, Q. Fan, Y. Gao, H. Wang, A. W. Robertson, S. Hong, Y. Jung, S. Liu, and Z. Sun. Nitrogen fixation by ru single-atom electrocatalytic reduction. *Chem*, 5(1):204–214, jan 2019.
77. M. A. Turchanin and P. G. Agraval. Cohesive energy, properties, and formation energy of transition metal alloys. *Powder Metallurgy and Metal Ceramics*, 47(1-2):26–39, jan 2008.
78. P. C. K. Vesborg and T. F. Jaramillo. Addressing the terawatt challenge: scalability in the supply of chemical elements for renewable energy. *RSC Advances*, 2(21):7933, 2012.
79. L. E. Walle, A. Borg, P. Uvdal, and A. Sandell. Experimental evidence for mixed dissociative and molecular adsorption of water on a rutile TiO₂ (110) surface without oxygen vacancies. *Physical Review B*, 80(23):235436, 2009.
80. L. Wang, M. Xia, H. Wang, K. Huang, C. Qian, C. T. Maravelias, and G. A. Ozin. Greening ammonia toward the solar ammonia refinery. *Joule*, 2(6):1055 – 1074, 2018.
81. S. Wang, V. Petzold, V. Tripkovic, J. Kleis, J. G. Howalt, E. Skúlason, E. M. Fernández, B. Hvolbæk, G. Jones, A. Toftelund, H. Falsig, M. Bjerketun, F. Studt, F. Abild-Pedersen, J. Rossmeisl, J. K. Nørskov, and T. Bligaard. Universal transition state scaling relations for (de)hydrogenation over transition metals. *Physical Chemistry Chemical Physics*, 13(46):20760, 2011.
82. J. Wellendorff, K. T. Lundgaard, A. Møgelhøj, V. Petzold, D. D. Landis, J. K. Nørskov, T. Bligaard, and K. W. Jacobsen. Density functionals for surface science: Exchange-correlation model development with bayesian error estimation. *Physical Review B*, 85(23):235149–235149, 2012.
83. Z. Xu and J. R. Kitchin. Relationships between the surface electronic and chemical properties of doped 4d and 5d late transition metal dioxides. *The Journal of Chemical Physics*, 142(10):104703, mar 2015.
84. Z. Yao and K. Reuter. First-principles computational screening of dopants to improve the deacon process over RuO₂. *ChemCatChem*, 10(2):465–469, dec 2017.
85. J. T. Yates, A. Szabó, and M. A. Henderson. The influence of surface defect sites on chemisorption and catalysis. In *Structure-Activity and Selectivity Relationships in Heterogeneous Catalysis, Proceedings of the ACS Symposium on Structure-Activity Relationships in Heterogeneous Catalysis*, pages 273–290. Elsevier, 1991.
86. J. Yu, J. Yu, Z. Shi, Q. Guo, X. Xiao, H. Mao, and D. Mao. The effects of the nature of TiO₂ supports on the catalytic performance of Rh–Mn/TiO₂ catalysts in the synthesis of C₂ oxygenates from syngas. *Catalysis Science & Technology*, 9(14):3675–3685, 2019.
87. S.-J. Yuan, J.-J. Chen, Z.-Q. Lin, W.-W. Li, G.-P. Sheng, and H.-Q. Yu. Nitrate formation from atmospheric nitrogen and oxygen photocatalysed by nano-sized titanium dioxide. *Nat. Commun.*, 4, 2013.
88. A. Zaleska. Doped-TiO₂: A review. *Recent Patents on Engineering*, 2(3):157–164, nov 2008.
89. Z. Zhao, S. Hong, C. Yan, C. Choi, Y. Jung, Y. Liu, S. Liu, X. Li, J. Qiu, and Z. Sun. Efficient visible-light driven n₂ fixation over two-dimensional sb/TiO₂ composites. *Chemical Communications*, 55(50):7171–7174, 2019.

Supplementary Information for Computational Study of Transition-Metal Substitutions in Rutile TiO₂ (110) for Photoelectrocatalytic Ammonia Synthesis

Benjamin M. Comer, Max H. Lenk, Aradhya P. Rajanala, Emma L. Flynn,
Andrew J. Medford

E-mail:

Table S1: The calculated relative energies of all 2+ surface species on all metal substituents at standard state. All energies are referenced with respect to N₂ gas and H₂ gas at 300K and 1 bar of pressure. Blank spaces represent calculations that could not be converged

Element	H ₂ NNH ₂	HNNH	N	N ₂	N ₂ H	N ₂ H ₂	N ₂ H ₃	NH	NH ₂	NH ₃	Formation Energy
Y	1.01	1.69	2.72	0.02		2.0	1.34	2.58	-0.15	-0.77	-1.38
Rh	1.16	1.3	1.86	-0.16	0.71	0.85	0.44	1.34	-1.06	-0.87	6.01
Pt		2.16	2.77	0.26	1.78	2.06	1.44	1.69	-0.1	-0.09	6.86
Ir	0.82	0.74	1.03	-0.7	0.26	0.19	-0.01	0.54	-1.52	-1.2	7.07
Ta	1.1	0.31	-0.99	-0.13	0.42	-0.32	-0.22	-0.95	-1.86	-0.85	1.69
Zr	1.23	1.39	1.71	-0.01	1.07	0.74	0.35	0.16	-1.26	-0.88	-0.51
Re	0.95	0.67	-1.5	-0.83	-0.42	-0.15	0.32	-0.18	-1.21	-0.96	5.06
Hf	1.21	1.32	1.59	-0.02	0.97	0.6	0.2	0.02	-1.44	-0.95	-0.92
Pd	1.53	2.12	3.55	0.23	2.0	2.25	1.67	2.5	0.26	-0.22	6.08
Ti	1.42	1.64	1.73	0.11	1.27	0.85	0.61	0.37	-0.99	-0.6	0.0
Ag	1.44	2.33	5.3	0.24	2.62	2.65	2.04	3.83	1.11	-0.18	7.28
Sc	1.06	1.76	3.51	0.03	1.7	1.59	1.0	2.18	-0.6	-0.76	-1.71
Ru	0.82	0.76	0.48	-0.83	0.64	0.17	0.57	0.86	-0.93	-1.13	5.45
Co	1.14	1.53	2.34	0.12	1.04	1.05	0.78	1.82	-0.74	-0.72	4.49
Nb	1.23	0.43	-1.04	-0.23	0.35	-0.36	-0.04	-0.84	-1.7	-0.86	1.5
Mo	1.27	1.11	-1.2	-0.33	0.01	-0.08	0.39	-0.24	-1.2	-0.75	3.26
Ni	1.75	1.94	3.35	0.17	1.64	1.9	1.09		-0.06	-0.43	5.58
Tc	1.03	0.95	-0.87	-0.65	0.06	0.27	0.65	0.52	-0.87	-0.92	4.58
Os	0.61	0.39	-0.7	-1.17	-0.15	-0.36	0.06	0.06	-1.44	-1.29	6.31
Cu	1.33	2.07	4.51	0.18	2.33	2.4	1.65	3.41	0.78	-0.45	6.55
V	1.43	1.5	-0.33	0.04	0.82	0.38	0.55	0.17	-1.04	-1.03	2.48
Au	1.68	2.36	4.05	0.25	2.54	2.82	2.15	2.95	0.75	-0.08	8.18
W	1.25	0.84	-1.8	-0.37	-0.24	-0.73	0.01	-1.06	-1.6	-0.8	3.99

Table S2: The calculated relative energies of all 4+ surface species on all metal substituents at standard state. All energies are referenced with respect to N₂ gas and H₂ gas at 300K and 1 bar of pressure. Blank spaces represent calculations that could not be converged

Element	N ₂	N ₂ H	Formation Energy
Y	0.04	2.6	1.1
Rh	-0.14	2.22	8.71
Pt	-0.34	1.77	10.08
Ir	-0.39	2.1	9.12
Ta	0.1	2.37	1.39
Zr	0.07	2.46	-0.75
Fe	-0.12		8.4
Hf	0.06	2.43	-1.22
Re	0.12		5.9
Pd	-0.01	1.7	9.88
Ti	0.16	2.54	-0.0
Ag	0.24		11.09
Sc	0.08	2.34	0.63
Ru	-0.0		7.5
Co	0.2		7.42
Nb	0.11	2.45	1.4
Mo	0.14		3.95
Ni	0.2	1.75	9.29
Tc	0.12		5.88
Os	-0.22	1.96	7.69
Cu	0.22		10.16
V	0.19	2.81	2.82
Au	0.27	2.23	11.22
W	0.13	2.37	4.36

Table S3: The limiting potentials and limiting steps for each dopant metal on 2+ surfaces

Element	Limiting Potential	Limiting Step
Sc	-1.7	$\text{N}_2 \rightarrow \text{N}_2\text{H}^*$
Ti	-1.27	$\text{N}_2 \rightarrow \text{N}_2\text{H}^*$
V	-0.82	$\text{N}_2 \rightarrow \text{N}_2\text{H}^*$
Co	-1.04	$\text{N}_2 \rightarrow \text{N}_2\text{H}^*$
Ni	-1.64	$\text{N}_2 \rightarrow \text{N}_2\text{H}^*$
Cu	-2.33	$\text{N}_2 \rightarrow \text{N}_2\text{H}^*$
Zr	-1.08	$\text{N}_2^* \rightarrow \text{N}_2\text{H}^*$
Nb	-1.38	$\text{NH}_2^* + \text{NH}_3 \rightarrow 2\text{NH}_3$
Mo	-0.89	$\text{NH}_2^* + \text{NH}_3 \rightarrow 2\text{NH}_3$
Tc	-0.71	$\text{N}_2^* \rightarrow \text{N}_2\text{H}^*$
Ru	-1.47	$\text{N}_2^* \rightarrow \text{N}_2\text{H}^*$
Rh	-0.88	$\text{N}_2^* \rightarrow \text{N}_2\text{H}^*$
Pd	-2.0	$\text{N}_2 \rightarrow \text{N}_2\text{H}^*$
Ag	-2.62	$\text{N}_2 \rightarrow \text{N}_2\text{H}^*$
Hf	-1.12	$\text{NH}_2^* + \text{NH}_3 \rightarrow 2\text{NH}_3$
Ta	-1.55	$\text{NH}_2^* + \text{NH}_3 \rightarrow 2\text{NH}_3$
W	-1.29	$\text{NH}_2^* + \text{NH}_3 \rightarrow 2\text{NH}_3$
Re	-0.9	$\text{NH}_2^* + \text{NH}_3 \rightarrow 2\text{NH}_3$
Os	-1.12	$\text{NH}_2^* + \text{NH}_3 \rightarrow 2\text{NH}_3$
Ir	-1.2	$\text{NH}_2^* + \text{NH}_3 \rightarrow 2\text{NH}_3$
Au	-2.54	$\text{N}_2 \rightarrow \text{N}_2\text{H}^*$

Table S4: The largest barrier for thermochemical steps and corresponding steps for each dopant metal on 2+ surfaces

Element	Largest Thermodynamic Step	Limiting Step
Sc	0.44	$\text{NH}_3^* + \text{NH}_3 \rightarrow 2\text{NH}_3$
Ti	0.68	$\text{NH}_3^* + \text{NH}_3 \rightarrow 2\text{NH}_3$
V	0.72	$\text{NH}_3^* + \text{NH}_3 \rightarrow 2\text{NH}_3$
Co	0.43	$\text{NH}_3^* + \text{NH}_3 \rightarrow 2\text{NH}_3$
Ni	0.17	$\text{N}_2 \rightarrow \text{N}_2^*$
Cu	1.25	$\text{H}_2\text{NNH}_2^* \rightarrow 2\text{NH}_2^*$
Zr	0.95	$\text{NH}_3^* + \text{NH}_3 \rightarrow 2\text{NH}_3$
Nb	1.38	$\text{NH}_3^* + \text{NH}_3 \rightarrow 2\text{NH}_3$
Mo	0.89	$\text{NH}_3^* + \text{NH}_3 \rightarrow 2\text{NH}_3$
Tc	0.61	$\text{NH}_3^* + \text{NH}_3 \rightarrow 2\text{NH}_3$
Ru	0.82	$\text{NH}_3^* + \text{NH}_3 \rightarrow 2\text{NH}_3$
Rh	0.75	$\text{NH}_3^* + \text{NH}_3 \rightarrow 2\text{NH}_3$
Pd	0.54	$\text{H}_2\text{NNH}_2^* \rightarrow 2\text{NH}_2^*$
Ag	1.48	$\text{H}_2\text{NNH}_2^* \rightarrow 2\text{NH}_2^*$
Hf	1.12	$\text{NH}_3^* + \text{NH}_3 \rightarrow 2\text{NH}_3$
Ta	1.55	$\text{NH}_3^* + \text{NH}_3 \rightarrow 2\text{NH}_3$
W	1.29	$\text{NH}_3^* + \text{NH}_3 \rightarrow 2\text{NH}_3$
Re	0.9	$\text{NH}_3^* + \text{NH}_3 \rightarrow 2\text{NH}_3$
Os	1.12	$\text{NH}_3^* + \text{NH}_3 \rightarrow 2\text{NH}_3$
Ir	1.2	$\text{NH}_3^* + \text{NH}_3 \rightarrow 2\text{NH}_3$
Au	0.88	$\text{H}_2\text{NNH}_2^* \rightarrow 2\text{NH}_2^*$

Table S5: The largest thermodynamic barrier and corresponding steps for each dopant metal on 2+ surfaces when set at the band edge of rutile, -0.142V

Element	Rate Limiting Step	Limiting Step
Sc	1.56	$\text{N}_2 \rightarrow \text{N}_2\text{H}^*$
Ti	1.13	$\text{N}_2 \rightarrow \text{N}_2\text{H}^*$
V	0.76	$\text{N}_2\text{H}_2^* \rightarrow \text{H}_2\text{NNH}_2^*$
Co	0.9	$\text{N}_2 \rightarrow \text{N}_2\text{H}^*$
Ni	1.62	$\text{N}_2 \rightarrow \text{N}_2\text{H}_2^*$
Cu	2.19	$\text{N}_2 \rightarrow \text{N}_2\text{H}^*$
Zr	0.94	$\text{N}_2^* \rightarrow \text{N}_2\text{H}^*$
Nb	1.31	$\text{N}_2\text{H}_2^* \rightarrow \text{H}_2\text{NNH}_2^*$
Mo	1.07	$\text{N}_2\text{H}_2^* \rightarrow \text{H}_2\text{NNH}_2^*$
Tc	1.11	$\text{N}_2^* \rightarrow \text{H}_2\text{NNH}_2^*$
Ru	1.33	$\text{N}_2^* \rightarrow \text{N}_2\text{H}^*$
Rh	0.73	$\text{N}_2^* \rightarrow \text{N}_2\text{H}^*$
Pd	1.96	$\text{N}_2 \rightarrow \text{N}_2\text{H}_2^*$
Ag	2.47	$\text{N}_2 \rightarrow \text{N}_2\text{H}^*$
Hf	0.98	$\text{NH}_2^* + \text{NH}_3 \rightarrow 2\text{NH}_3$
Ta	1.41	$\text{NH}_2^* + \text{NH}_3 \rightarrow 2\text{NH}_3$
W	1.69	$\text{N}_2\text{H}_2^* \rightarrow \text{H}_2\text{NNH}_2^*$
Re	1.21	$\text{N}_2^* \rightarrow \text{H}_2\text{NNH}_2^*$
Os	0.98	$\text{NH}_2^* + \text{NH}_3 \rightarrow 2\text{NH}_3$
Ir	1.06	$\text{NH}_2^* + \text{NH}_3 \rightarrow 2\text{NH}_3$
Au	2.54	$\text{N}_2 \rightarrow \text{N}_2\text{H}_2^*$

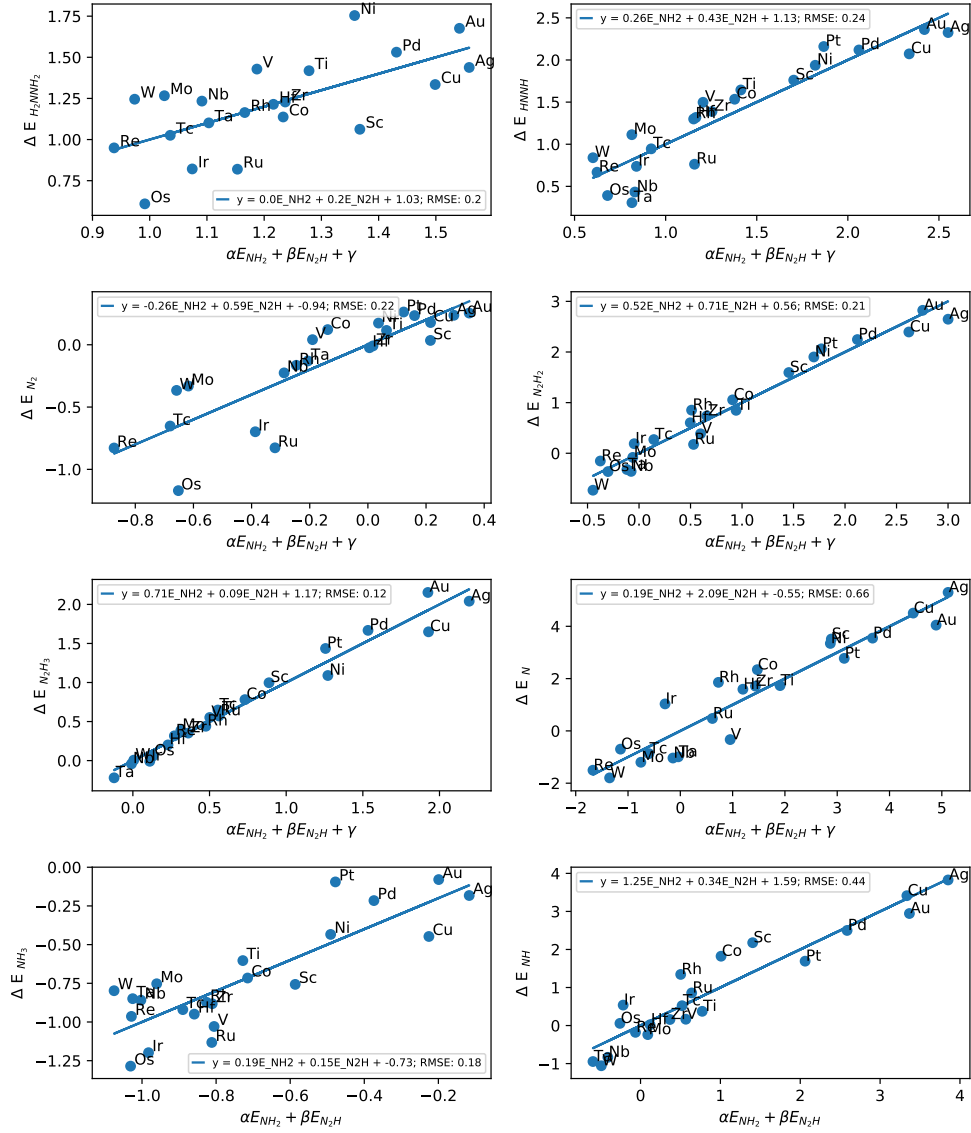


Figure S1: The calculated scaling relations between the binding energies of various species and the binding energies of N_2H and NH_2 on 2+ dopant sites

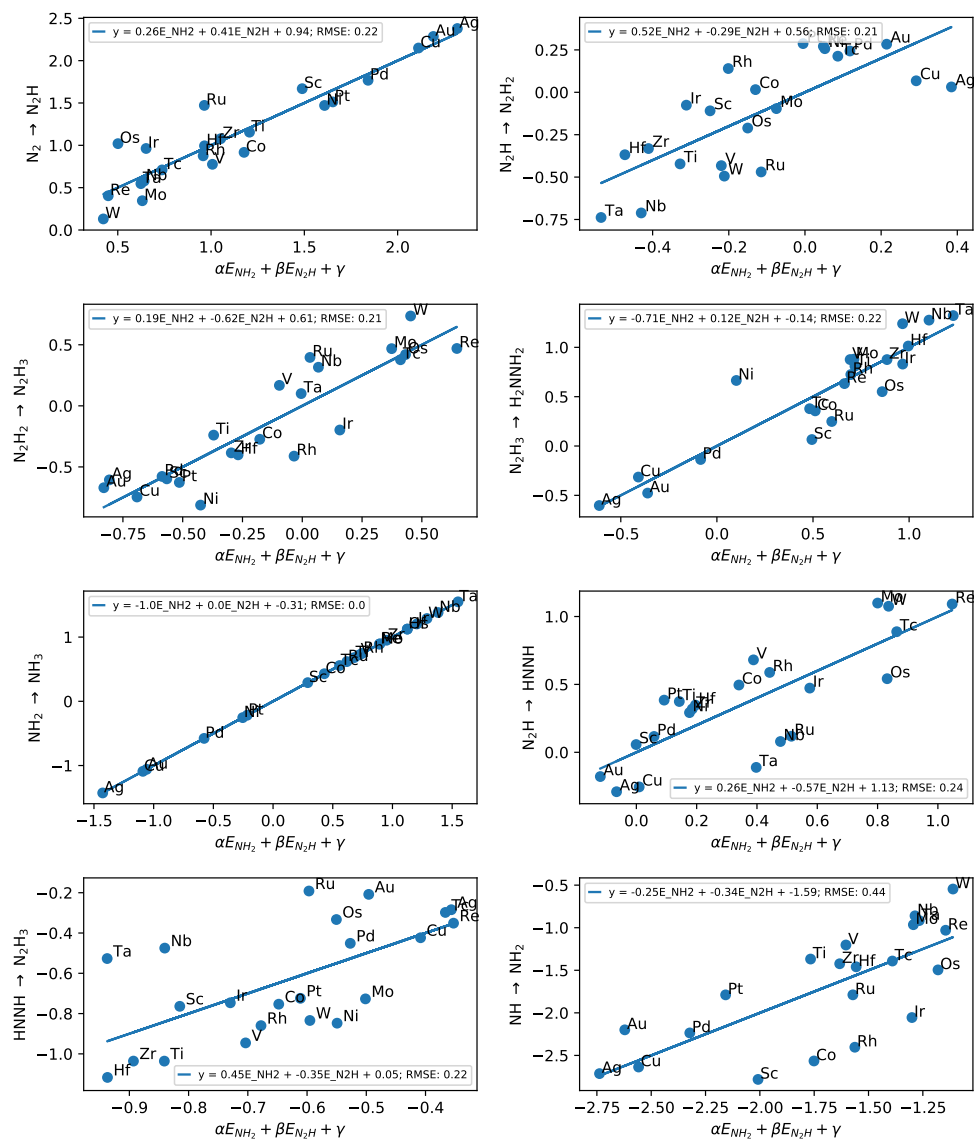


Figure S2: The calculated scaling relations between the reaction energies energies of all electrochemical reactions and the binding energies of N_2H and NH_2 on 2+ dopant sites

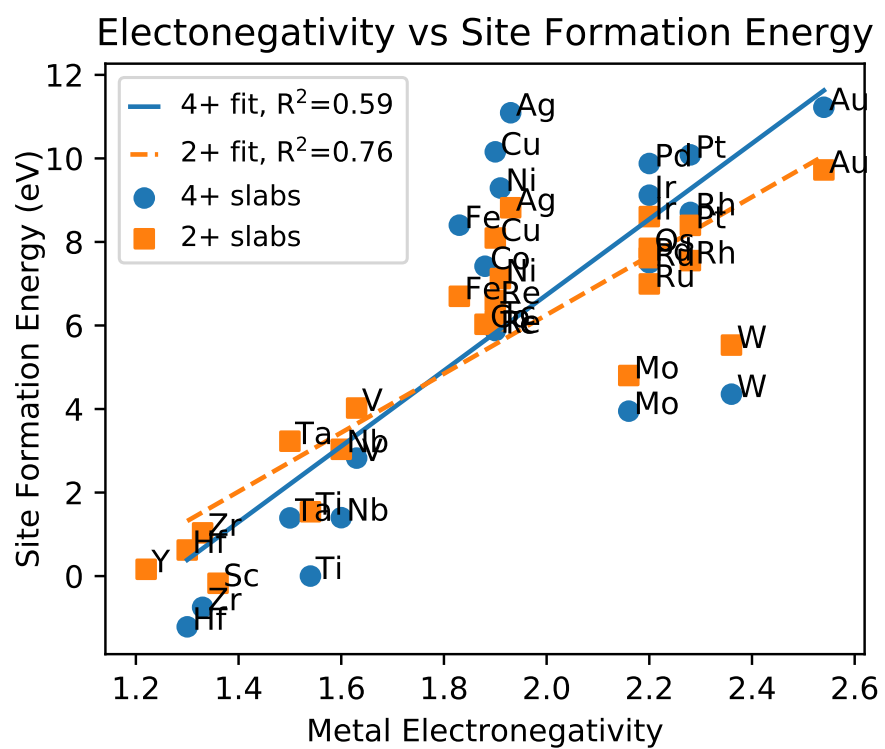


Figure S3: Electronegativity vs formation energy of 2+ dopant site

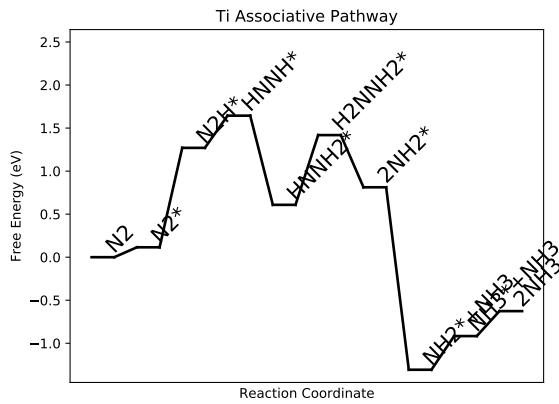


Figure S4: Free energy diagram for Ti

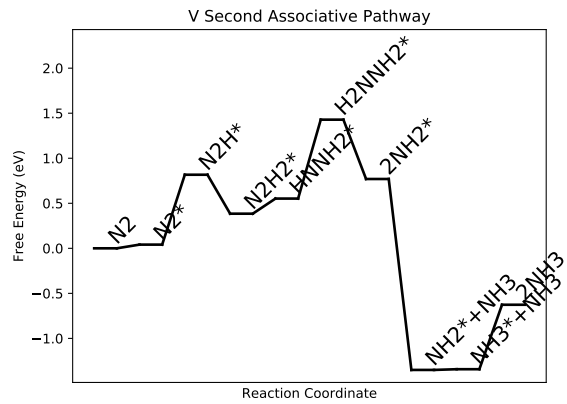


Figure S6: Free energy diagram for V

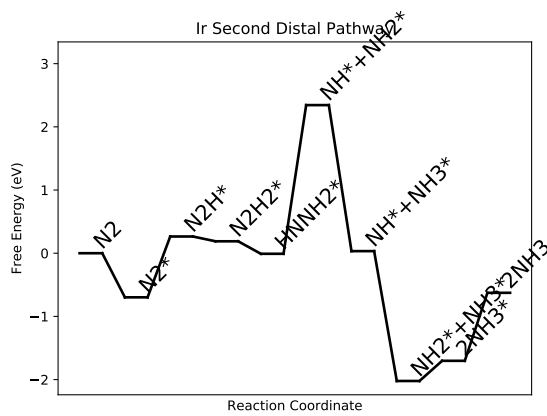


Figure S5: Free energy diagram for Ir

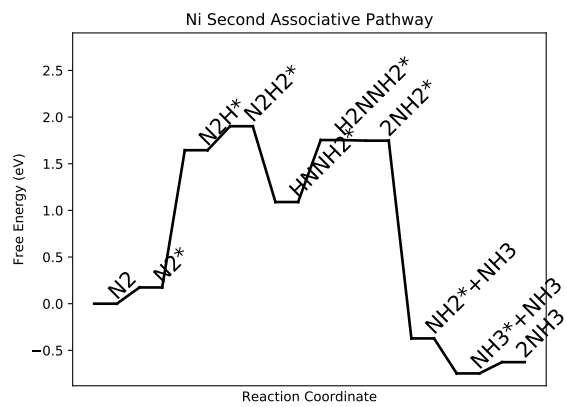


Figure S7: Free energy diagram for Ni

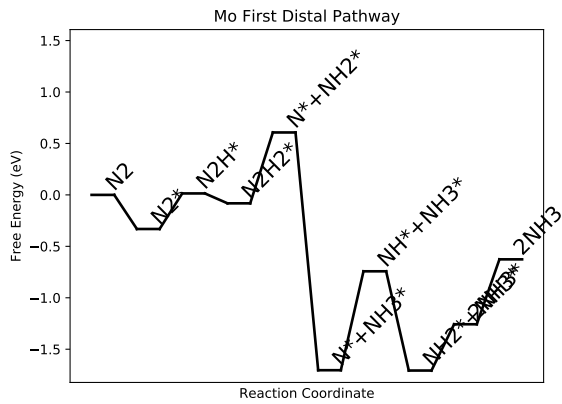


Figure S8: Free energy diagram for Mo

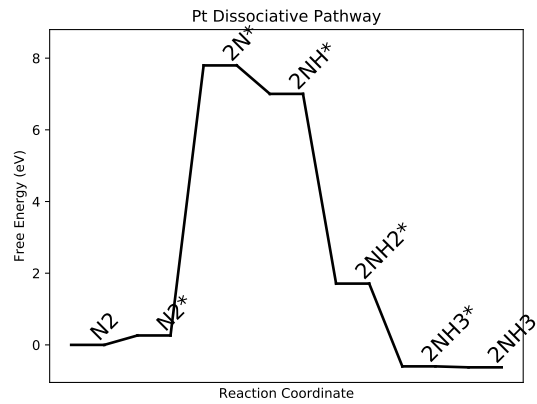


Figure S10: Free energy diagram for Pt

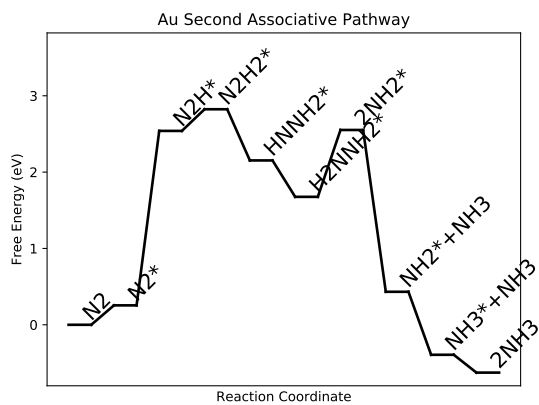


Figure S9: Free energy diagram for Au

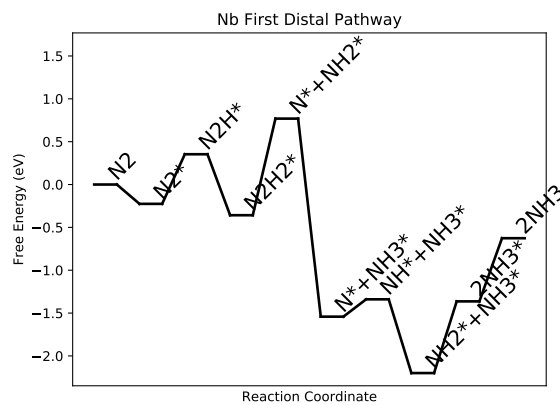


Figure S11: Free energy diagram for Nb

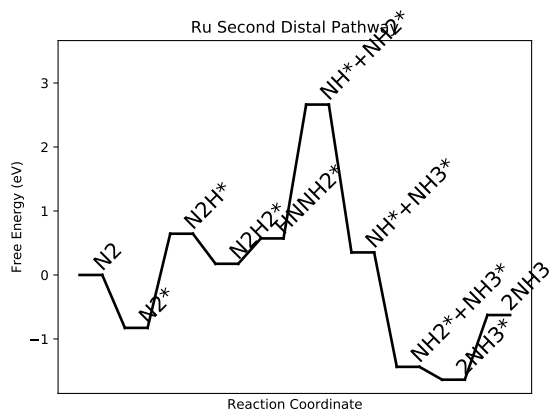


Figure S12: Free energy diagram for Ru

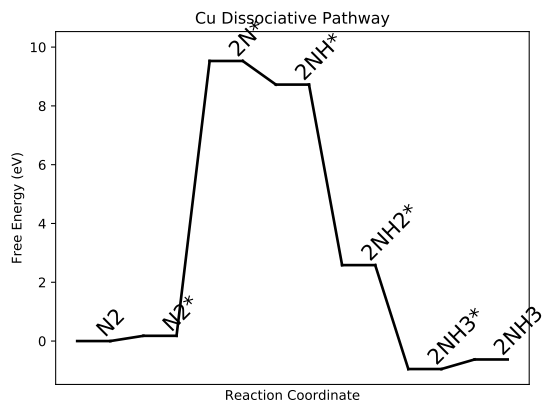


Figure S14: Free energy diagram for Cu

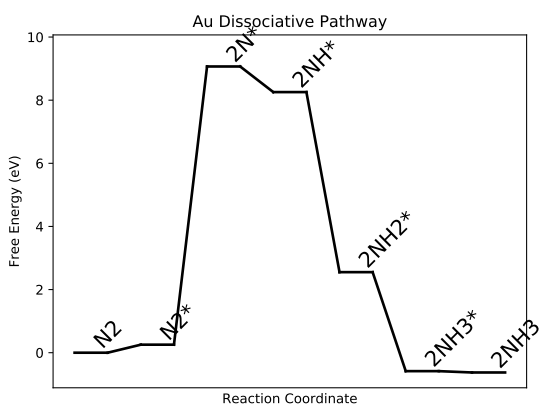


Figure S13: Free energy diagram for Au

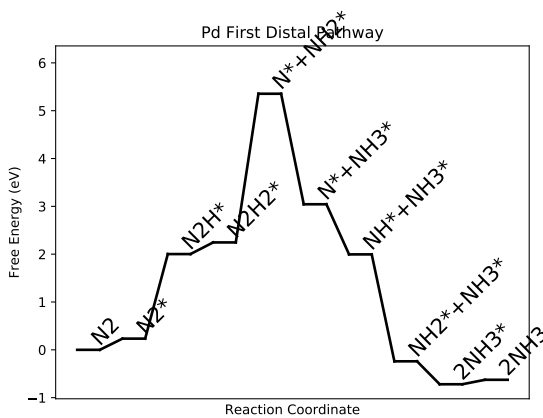


Figure S15: Free energy diagram for Pd

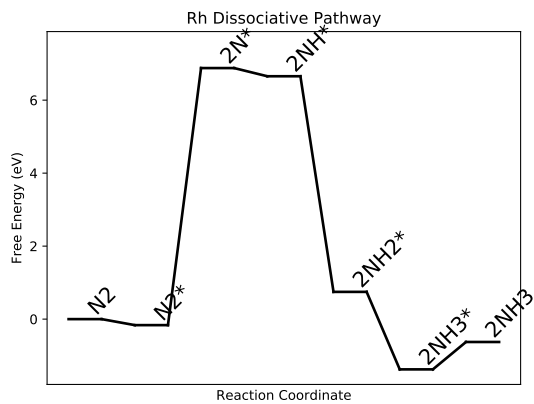


Figure S16: Free energy diagram for Rh

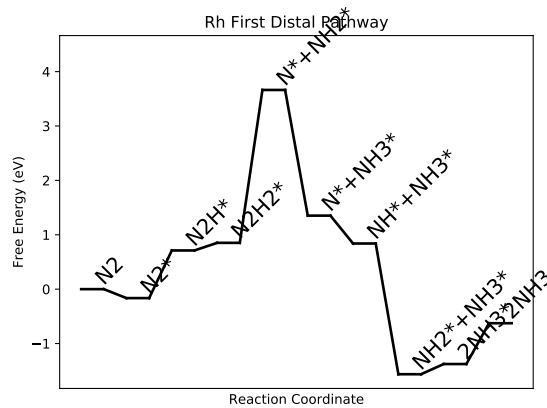


Figure S18: Free energy diagram for Rh

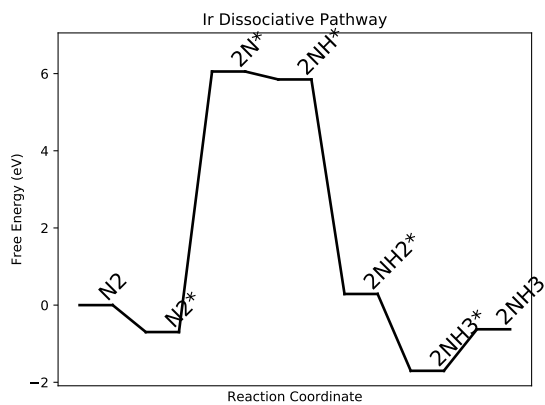


Figure S17: Free energy diagram for Ir

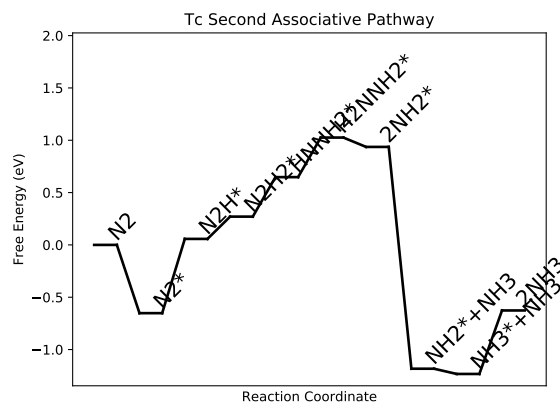


Figure S19: Free energy diagram for Tc

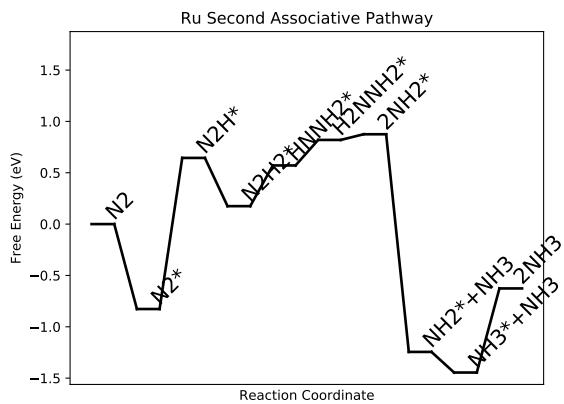


Figure S20: Free energy diagram for Ru

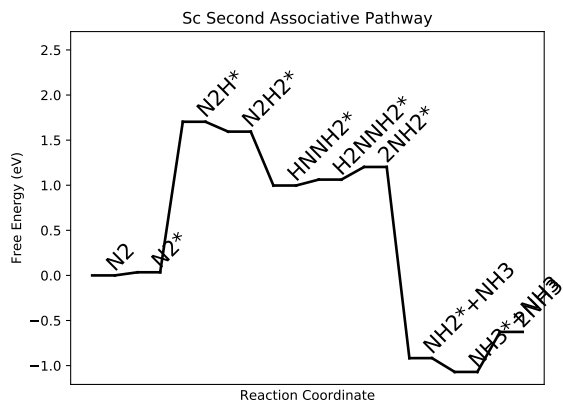


Figure S22: Free energy diagram for Sc

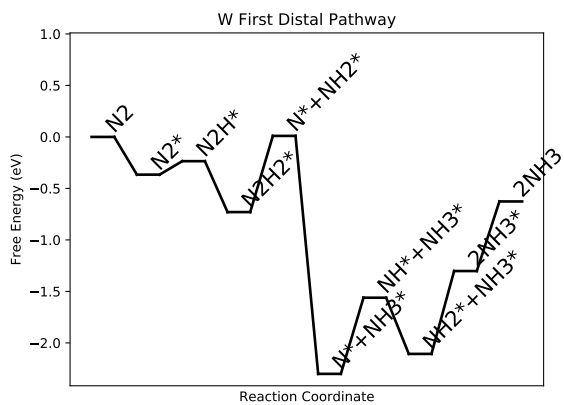


Figure S21: Free energy diagram for W

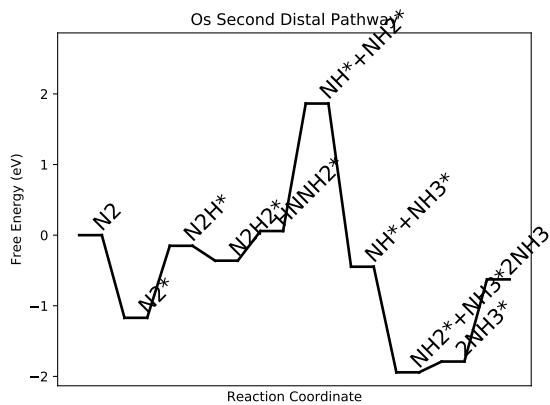


Figure S23: Free energy diagram for Os

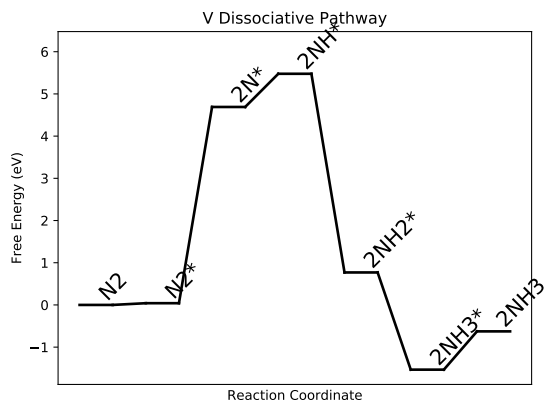


Figure S24: Free energy diagram for V

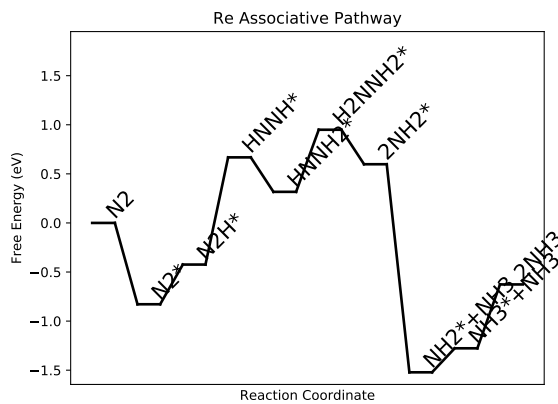


Figure S26: Free energy diagram for Re

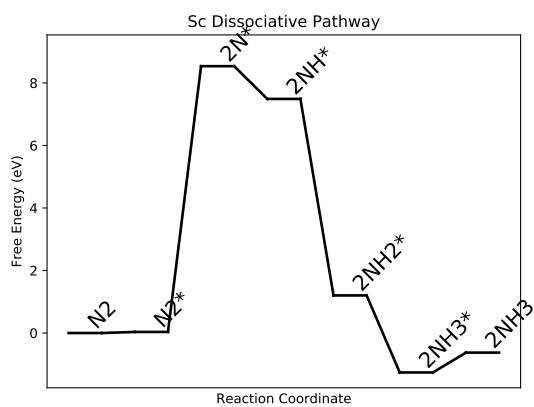


Figure S25: Free energy diagram for Sc

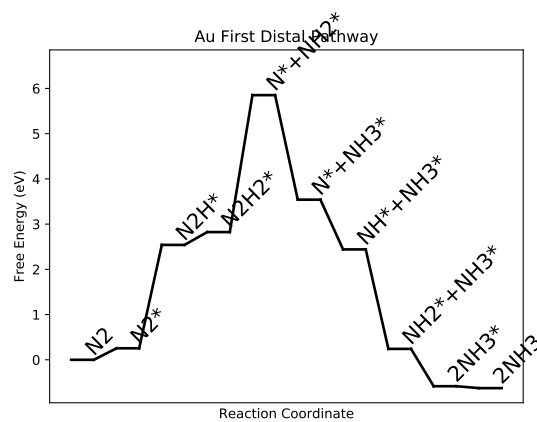


Figure S27: Free energy diagram for Au

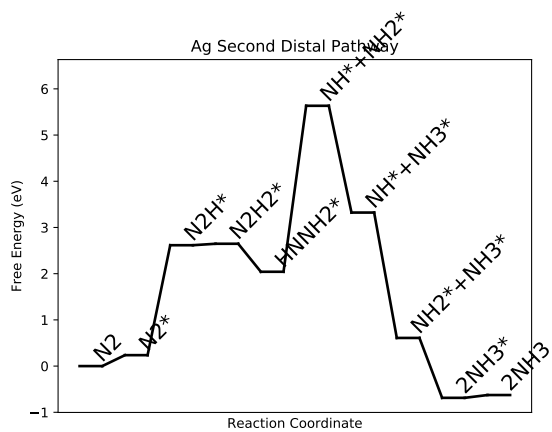


Figure S28: Free energy diagram for Ag

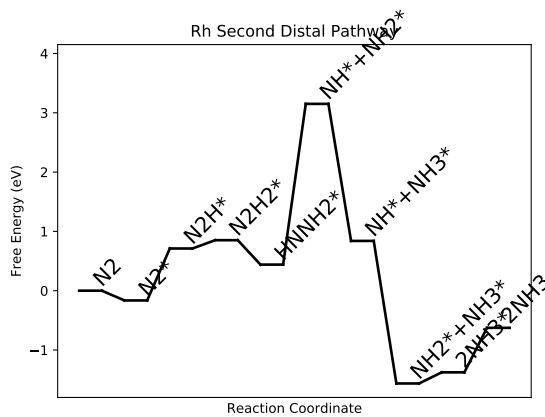


Figure S30: Free energy diagram for Rh

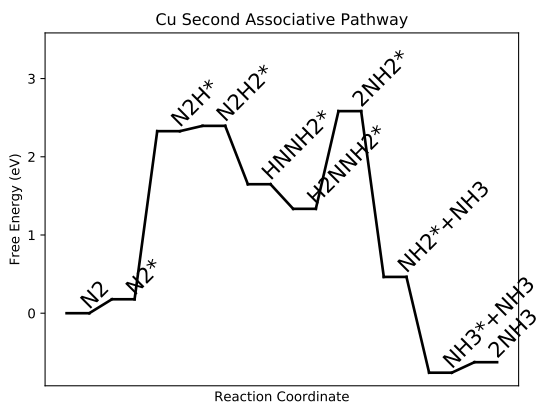


Figure S29: Free energy diagram for Cu

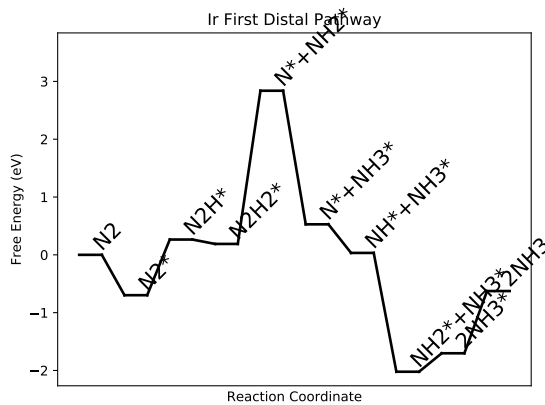


Figure S31: Free energy diagram for Ir

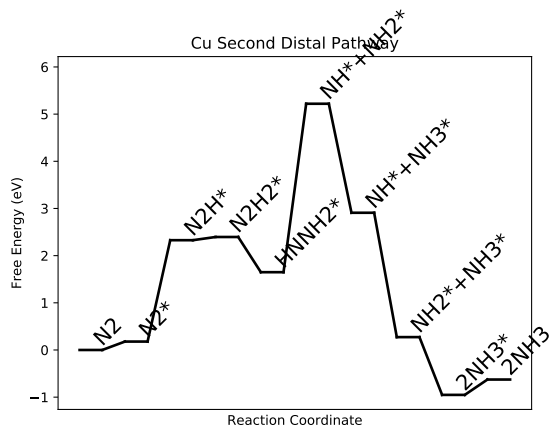


Figure S32: Free energy diagram for Cu

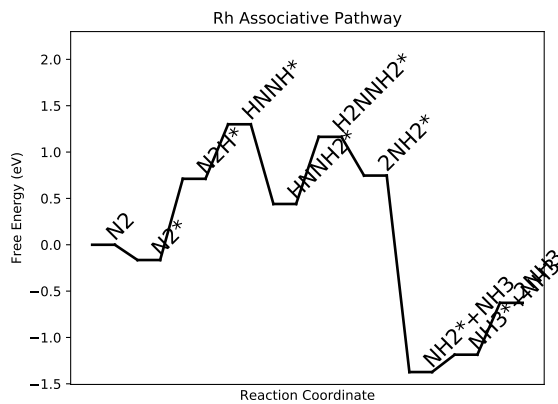


Figure S34: Free energy diagram for Rh

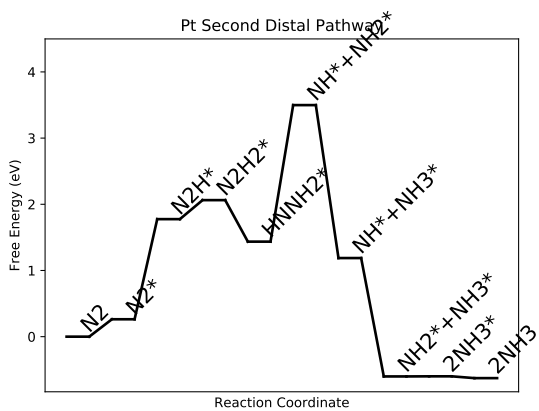


Figure S33: Free energy diagram for Pt

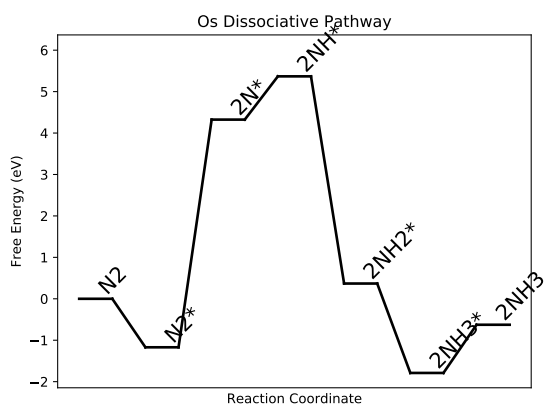


Figure S35: Free energy diagram for Os

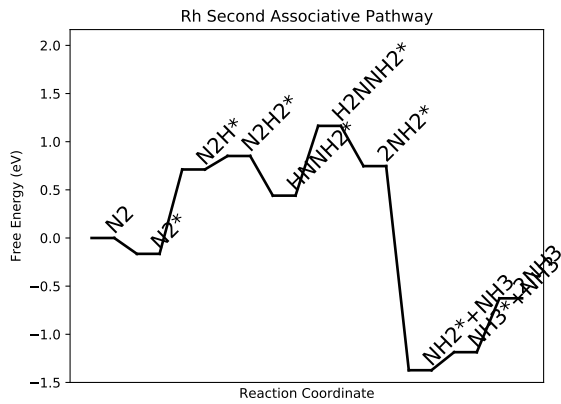


Figure S36: Free energy diagram for Rh

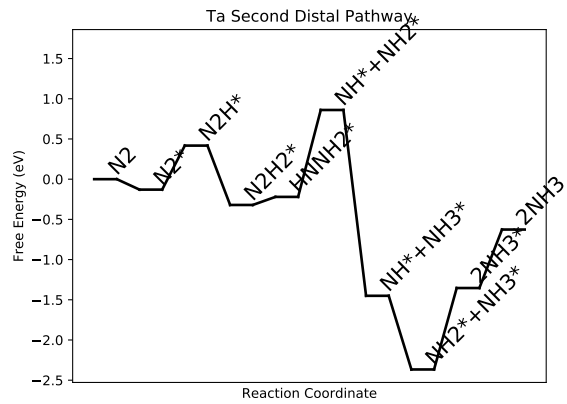


Figure S38: Free energy diagram for Ta

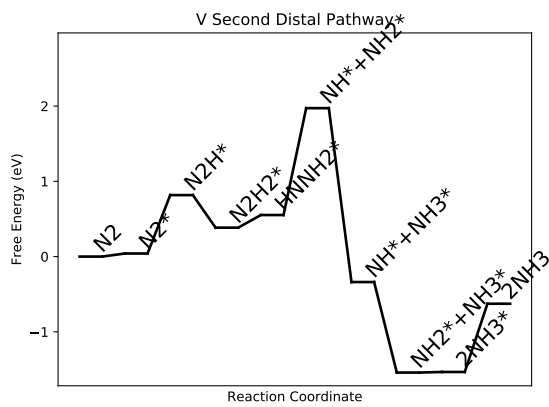


Figure S37: Free energy diagram for V

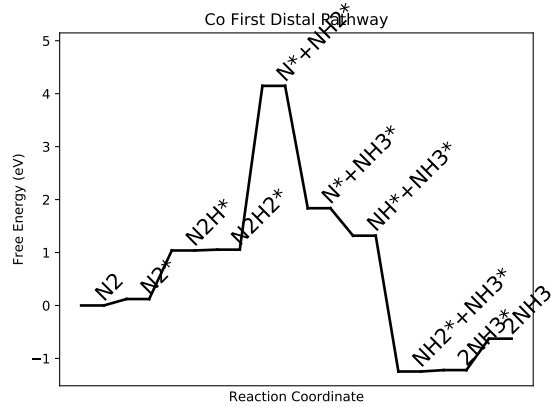


Figure S39: Free energy diagram for Co

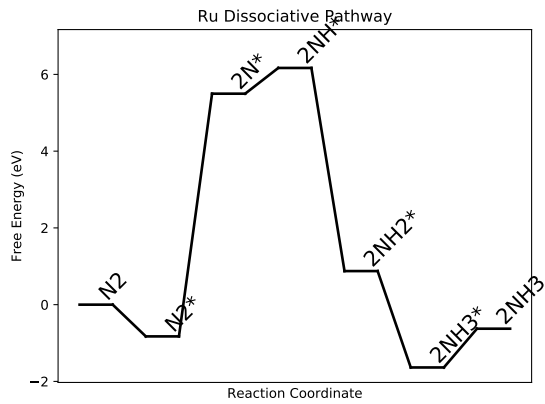


Figure S40: Free energy diagram for Ru

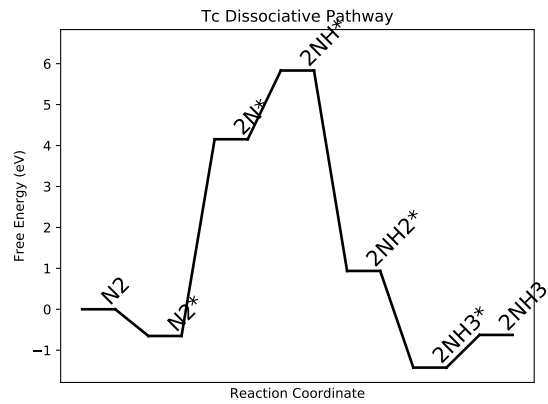


Figure S42: Free energy diagram for Tc

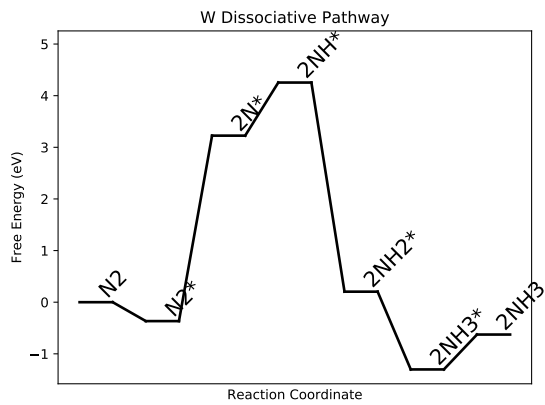


Figure S41: Free energy diagram for W

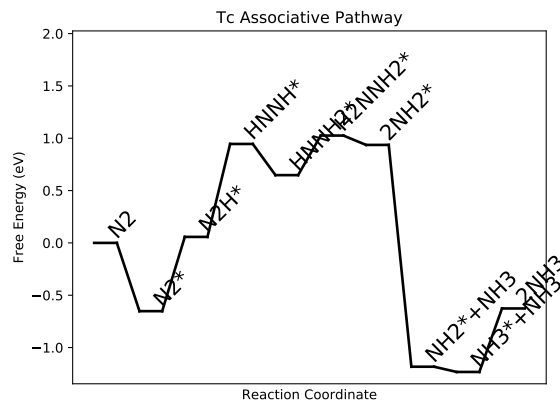


Figure S43: Free energy diagram for Tc

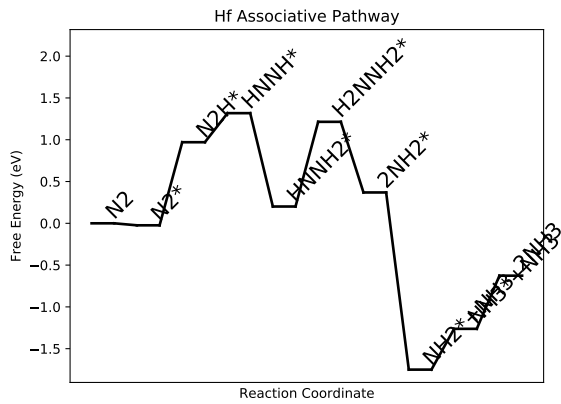


Figure S44: Free energy diagram for Hf

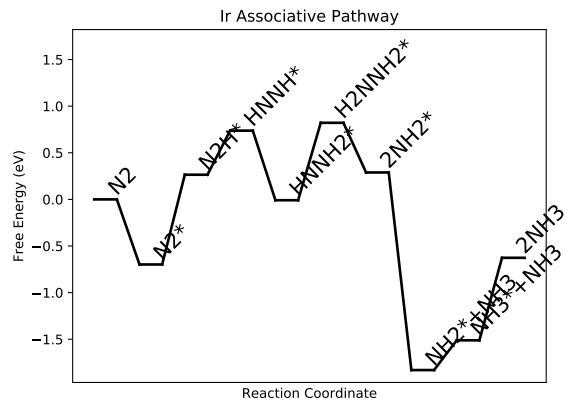


Figure S46: Free energy diagram for Ir

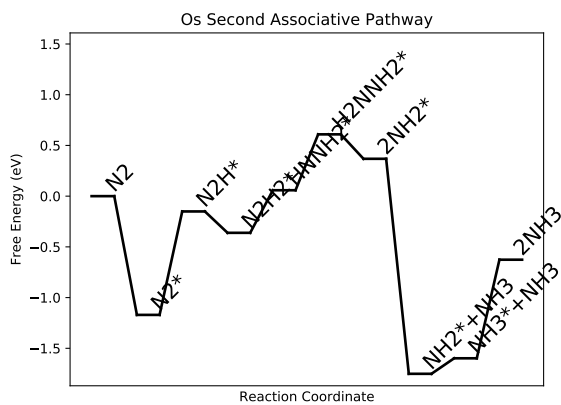


Figure S45: Free energy diagram for Os

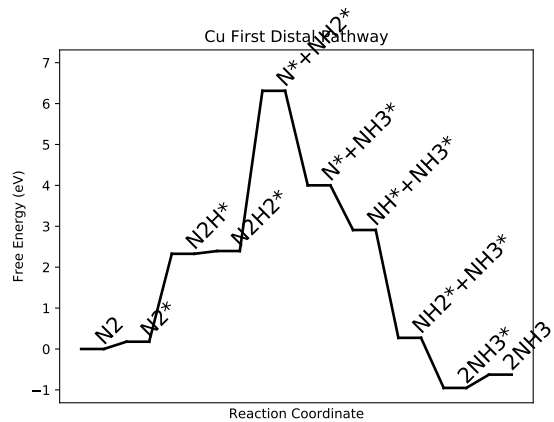


Figure S47: Free energy diagram for Cu

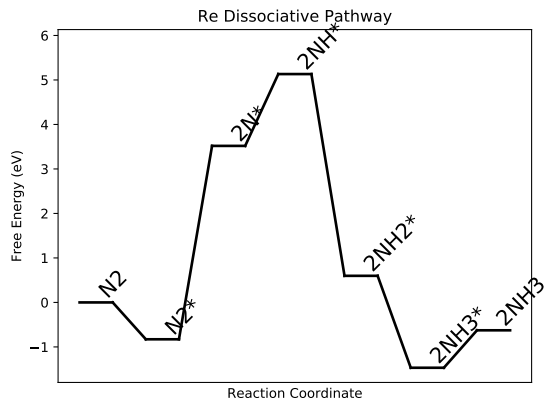


Figure S48: Free energy diagram for Re

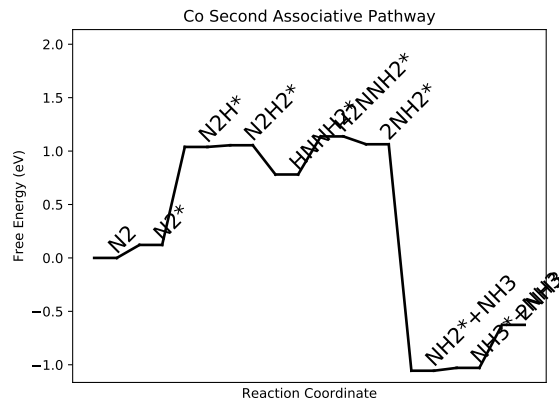


Figure S50: Free energy diagram for Co

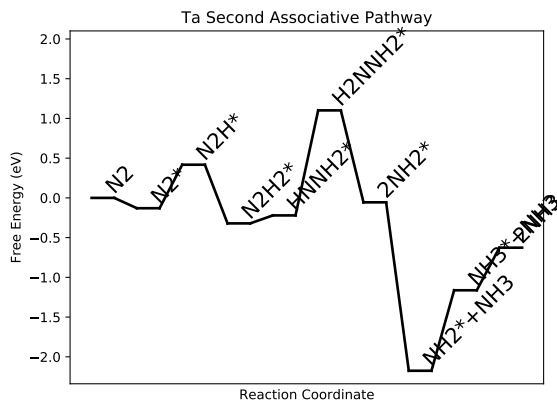


Figure S49: Free energy diagram for Ta

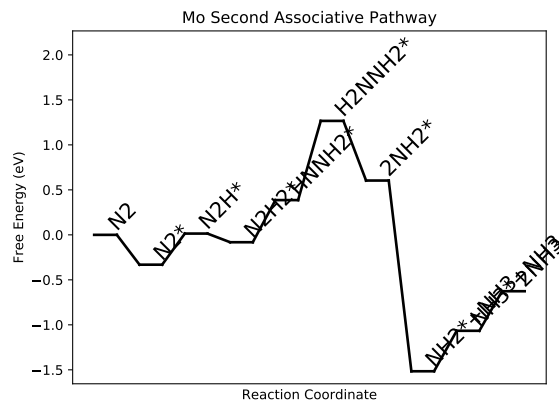


Figure S51: Free energy diagram for Mo

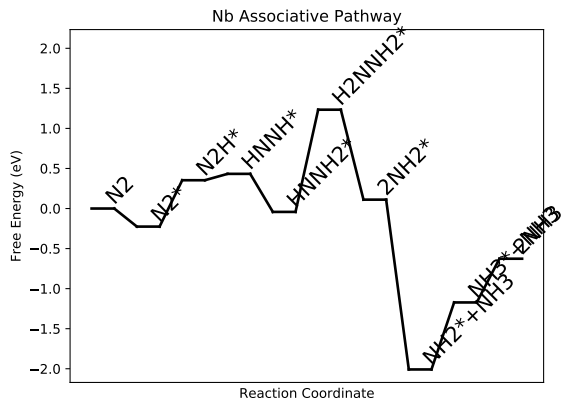


Figure S52: Free energy diagram for Nb

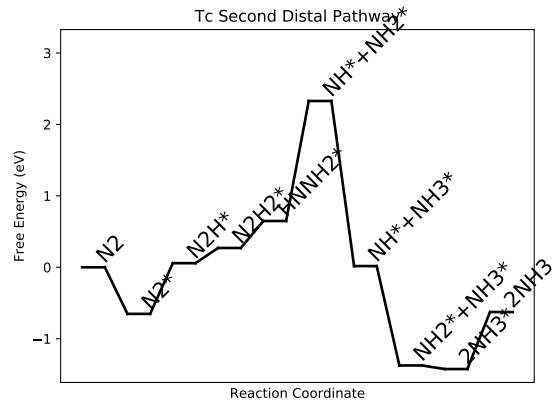


Figure S54: Free energy diagram for Tc

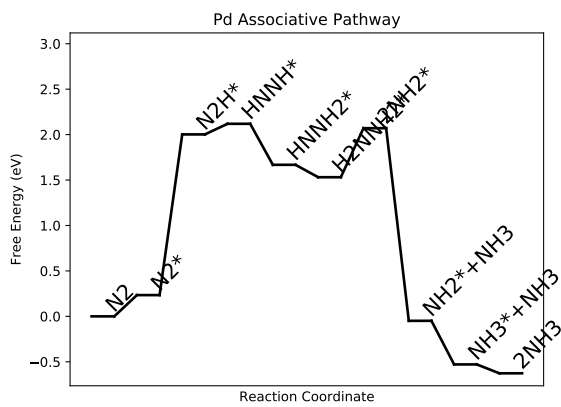


Figure S53: Free energy diagram for Pd

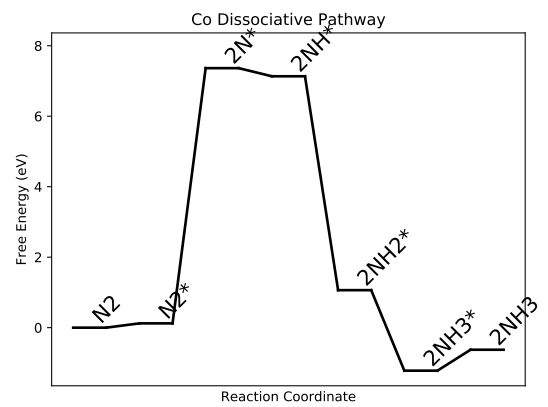


Figure S55: Free energy diagram for Co

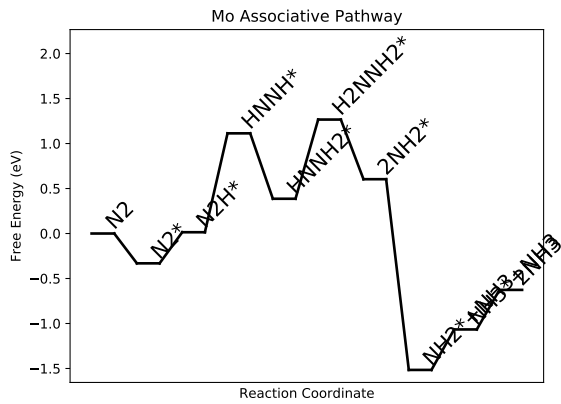


Figure S56: Free energy diagram for Mo

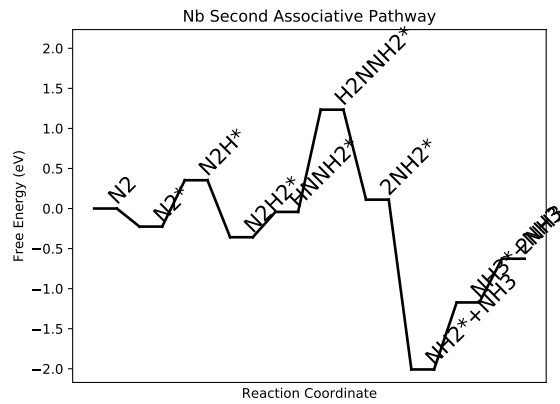


Figure S58: Free energy diagram for Nb

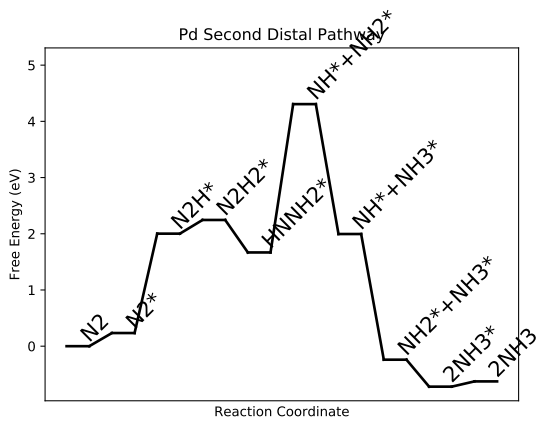


Figure S57: Free energy diagram for Pd

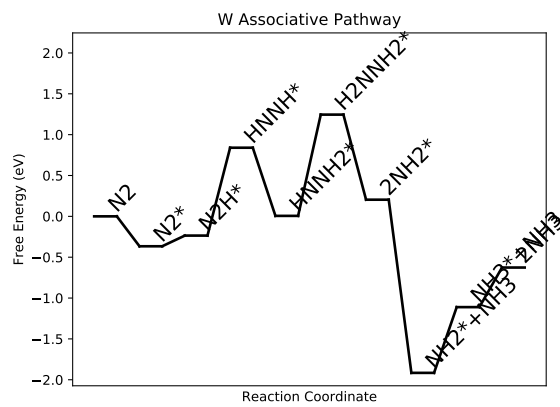


Figure S59: Free energy diagram for W

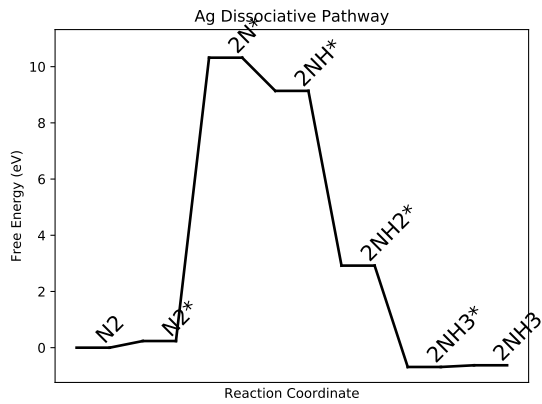


Figure S60: Free energy diagram for Ag

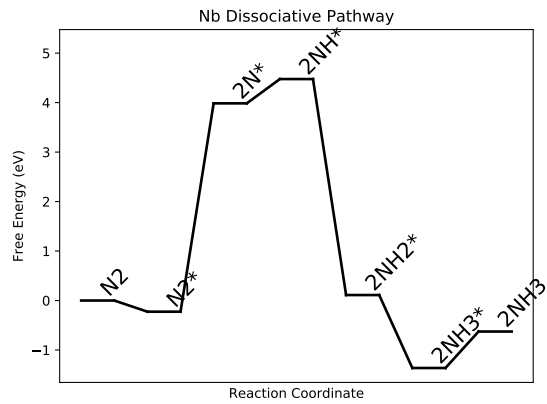


Figure S62: Free energy diagram for Nb

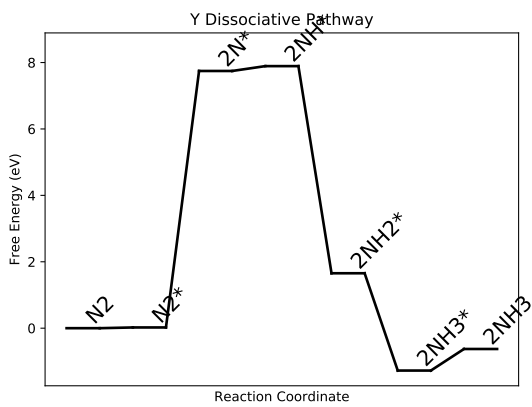


Figure S61: Free energy diagram for Y

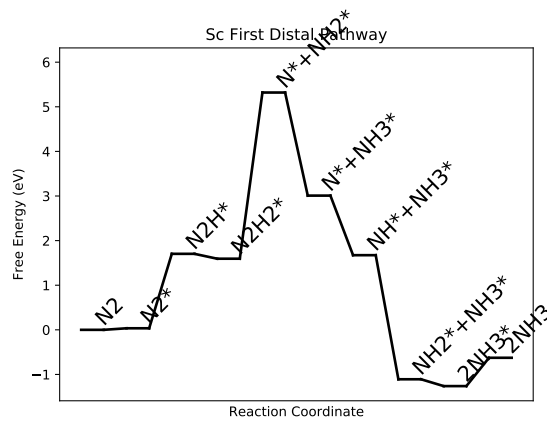


Figure S63: Free energy diagram for Sc

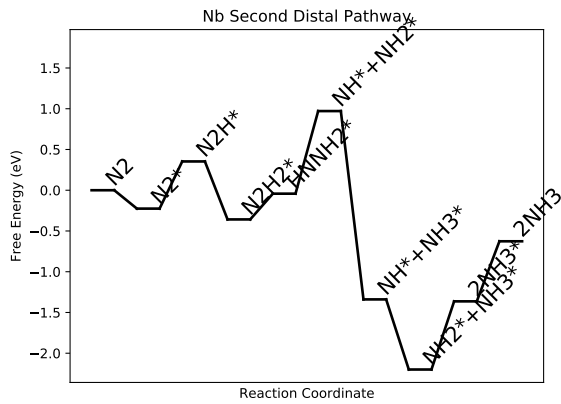


Figure S64: Free energy diagram for Nb

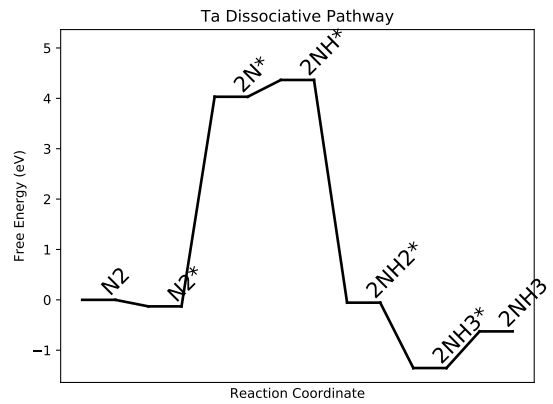


Figure S66: Free energy diagram for Ta

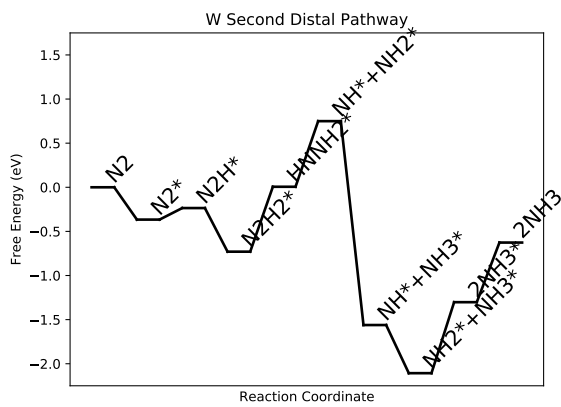


Figure S65: Free energy diagram for W

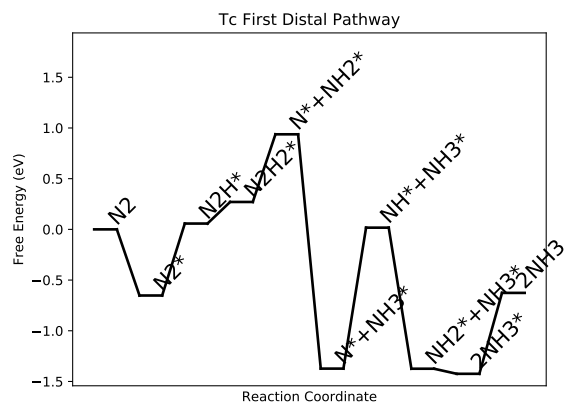


Figure S67: Free energy diagram for Tc

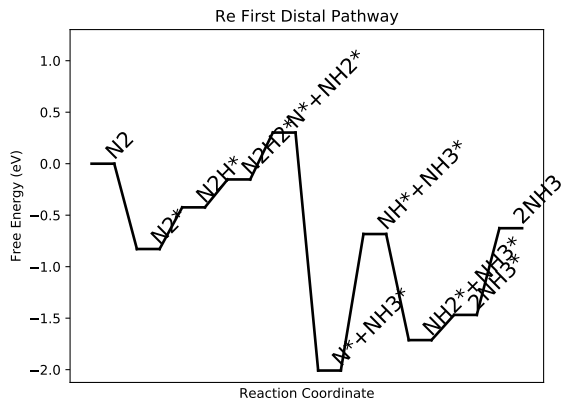


Figure S68: Free energy diagram for Re

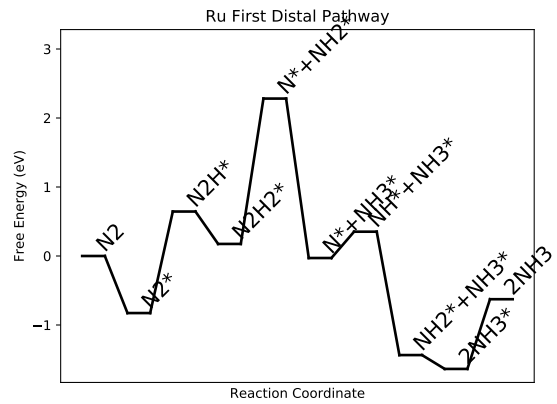


Figure S70: Free energy diagram for Ru

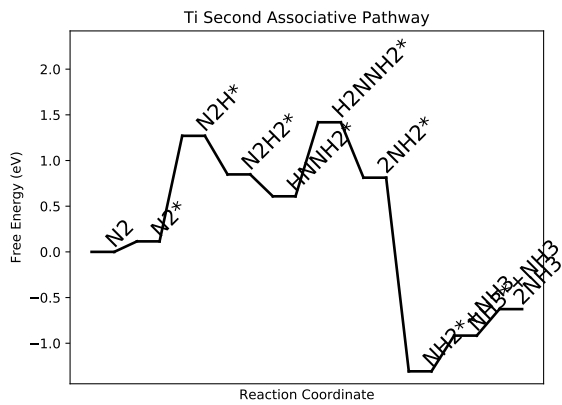


Figure S69: Free energy diagram for Ti

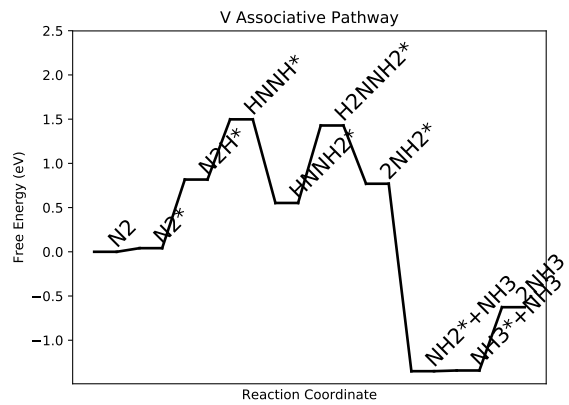


Figure S71: Free energy diagram for V

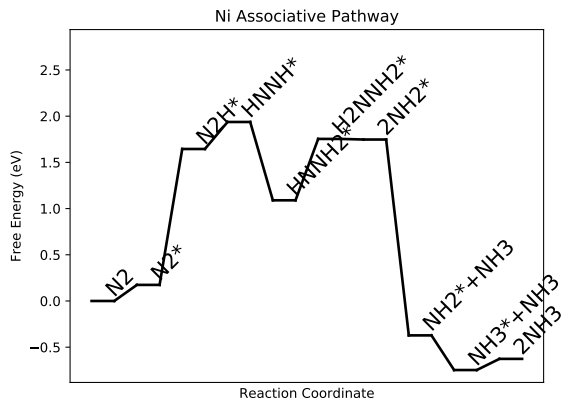


Figure S72: Free energy diagram for Ni

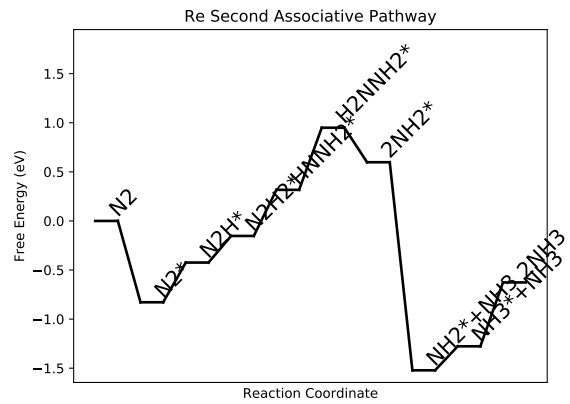


Figure S74: Free energy diagram for Re

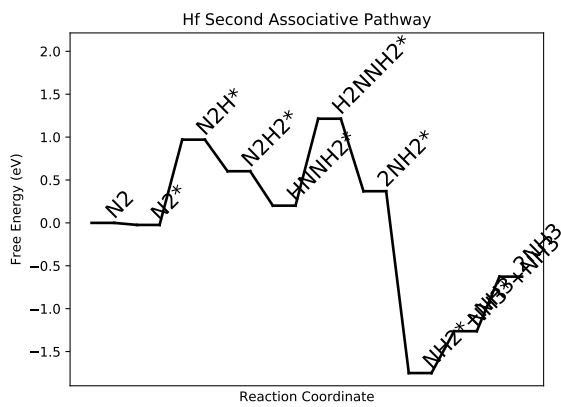


Figure S73: Free energy diagram for Hf

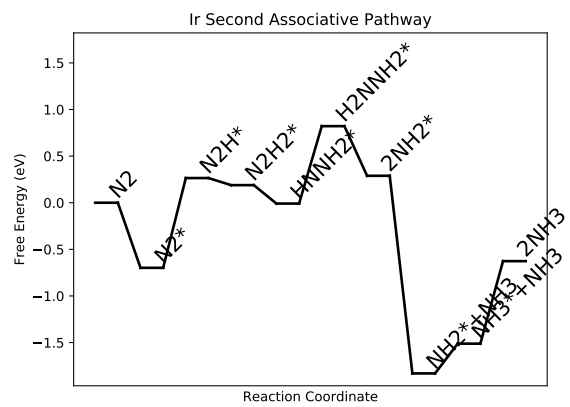


Figure S75: Free energy diagram for Ir

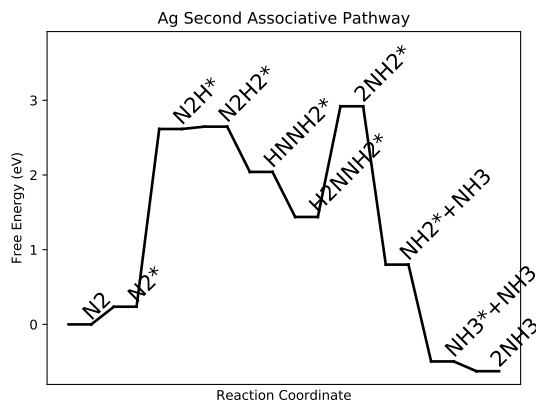


Figure S76: Free energy diagram for Ag

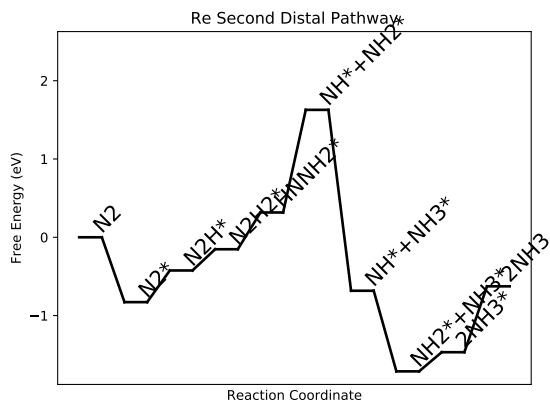


Figure S78: Free energy diagram for Re

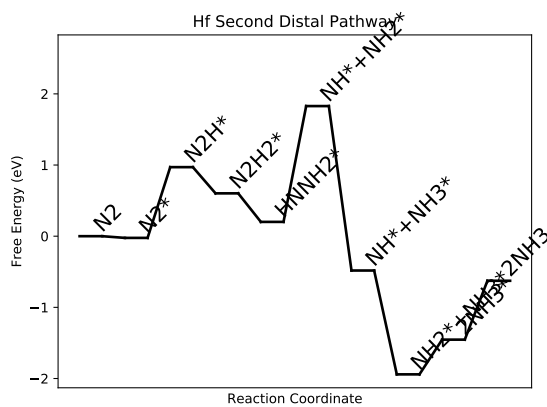


Figure S77: Free energy diagram for Hf

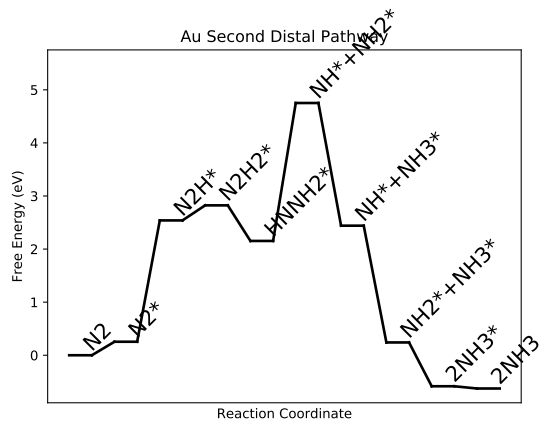


Figure S79: Free energy diagram for Au

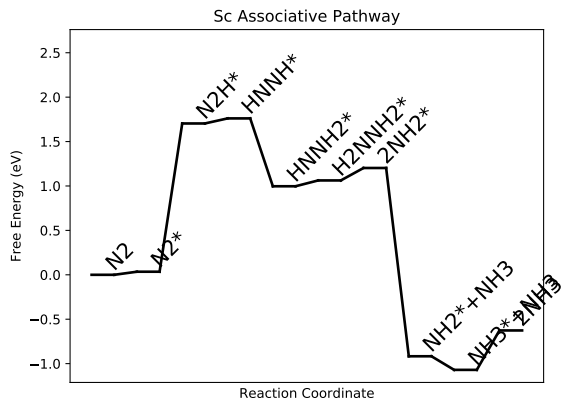


Figure S80: Free energy diagram for Sc

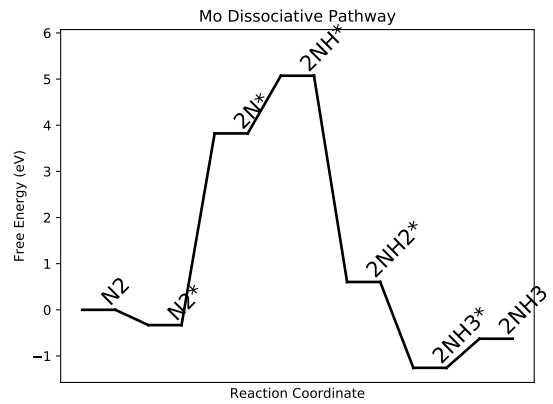


Figure S82: Free energy diagram for Mo

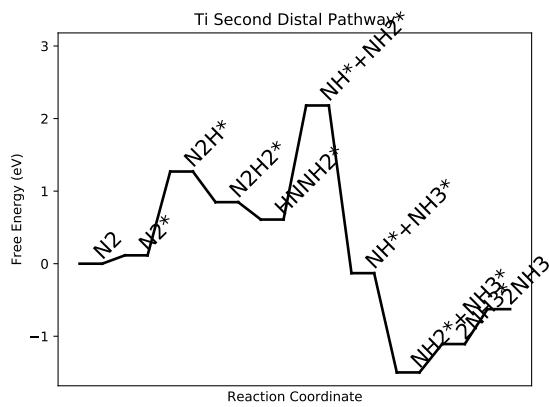


Figure S81: Free energy diagram for Ti

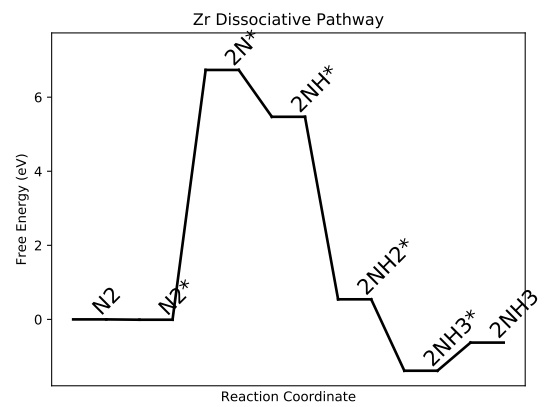


Figure S83: Free energy diagram for Zr

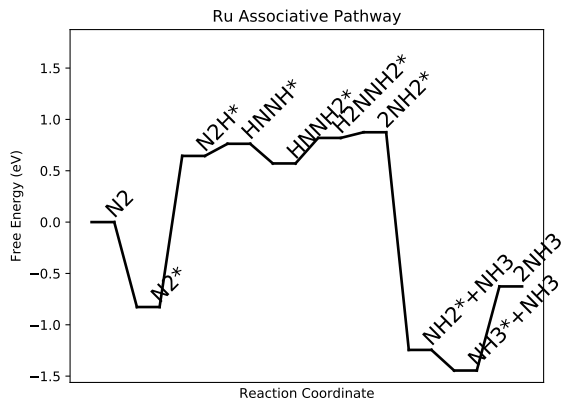


Figure S84: Free energy diagram for Ru

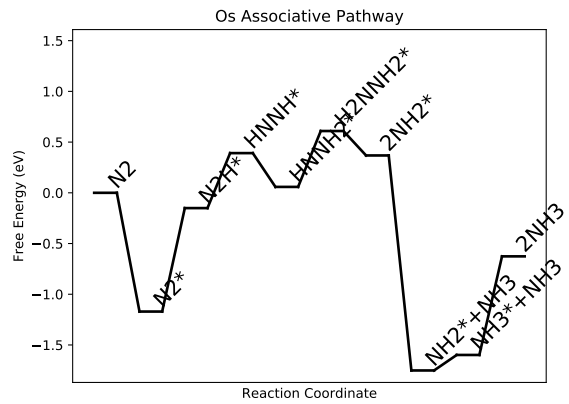


Figure S86: Free energy diagram for Os

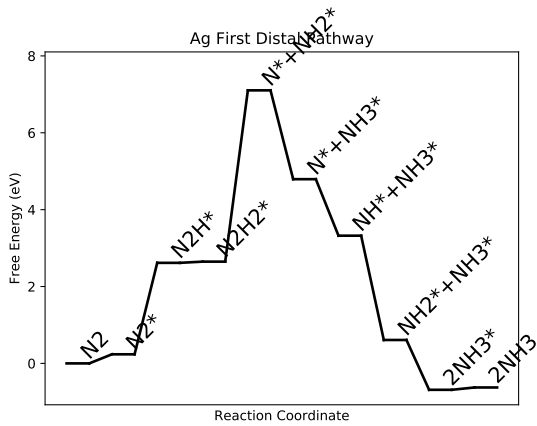


Figure S85: Free energy diagram for Ag

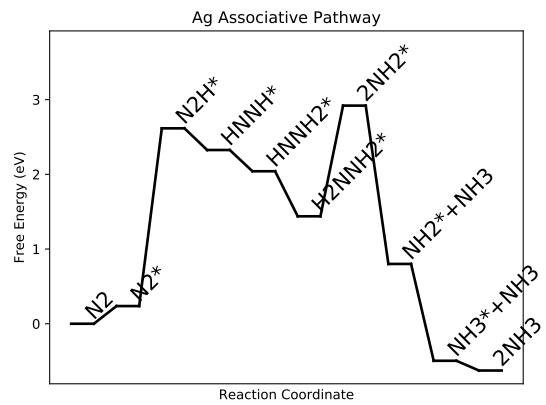


Figure S87: Free energy diagram for Ag

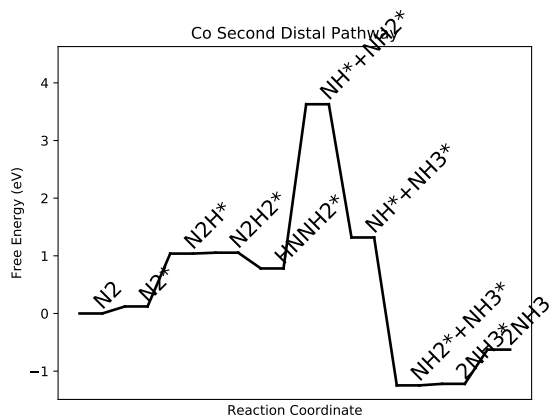


Figure S88: Free energy diagram for Co

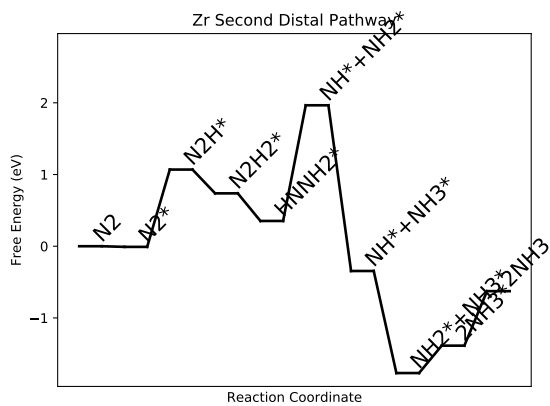


Figure S90: Free energy diagram for Zr

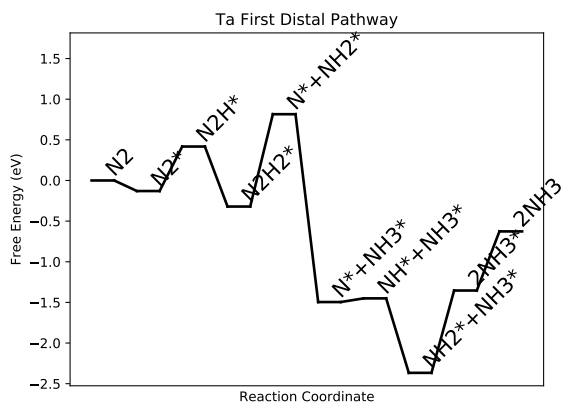


Figure S89: Free energy diagram for Ta

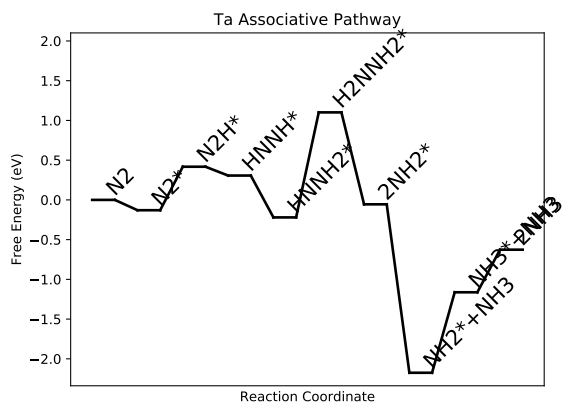


Figure S91: Free energy diagram for Ta

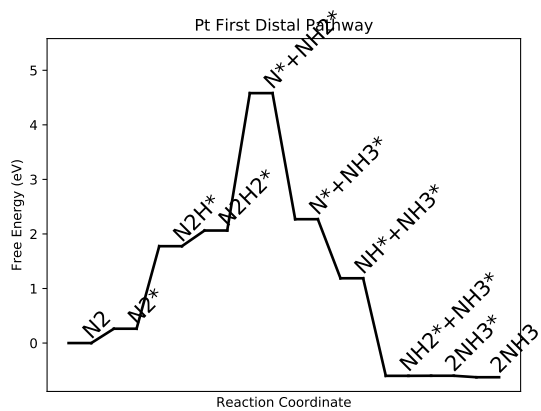


Figure S92: Free energy diagram for Pt

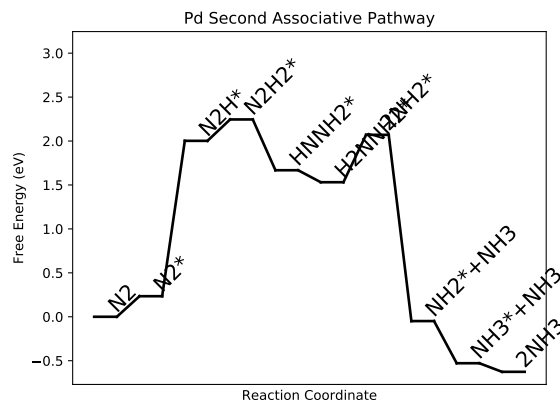


Figure S94: Free energy diagram for Pd

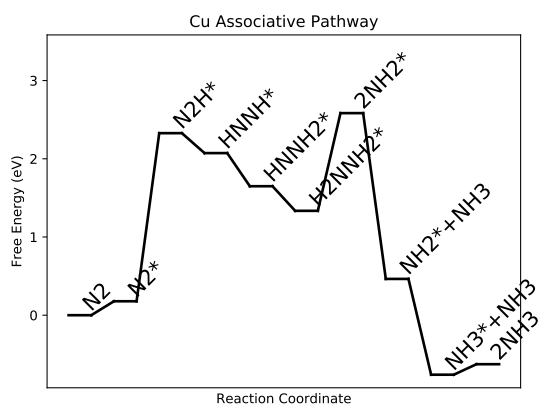


Figure S93: Free energy diagram for Cu

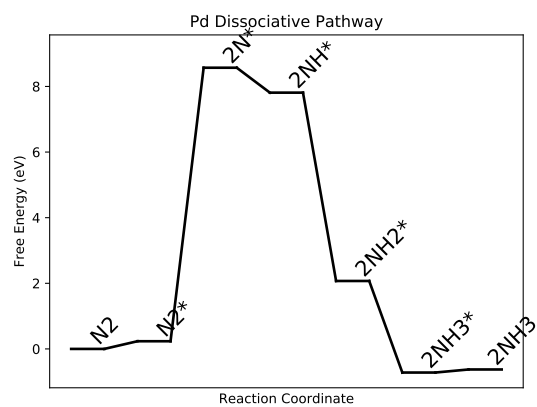


Figure S95: Free energy diagram for Pd

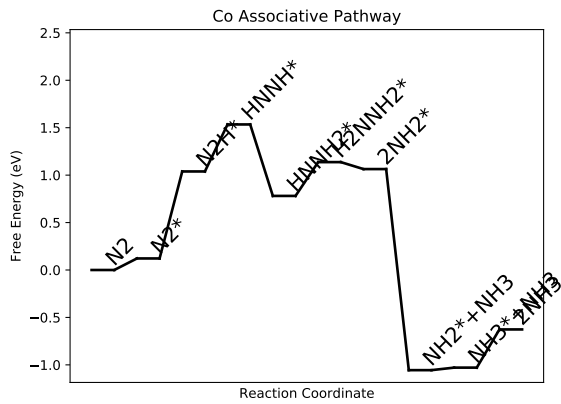


Figure S96: Free energy diagram for Co

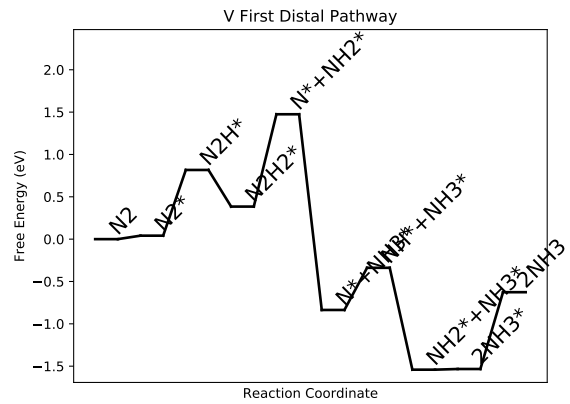


Figure S98: Free energy diagram for V

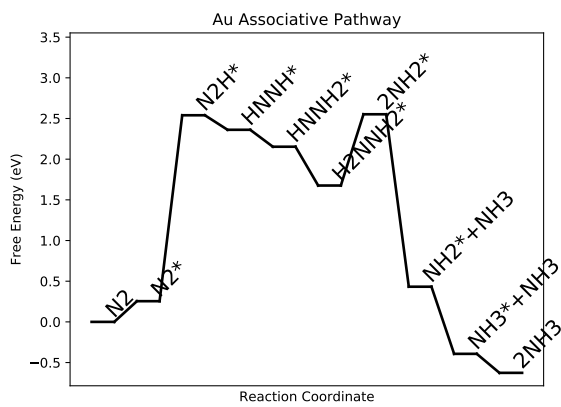


Figure S97: Free energy diagram for Au

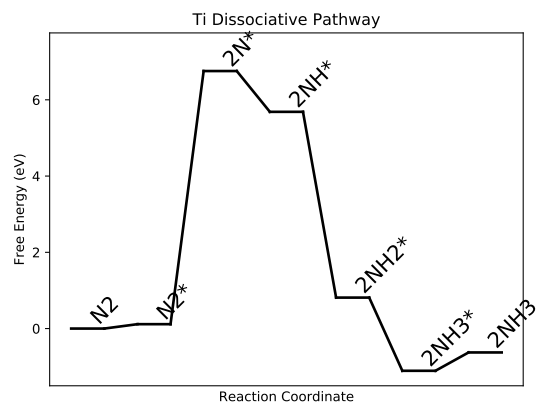


Figure S99: Free energy diagram for Ti

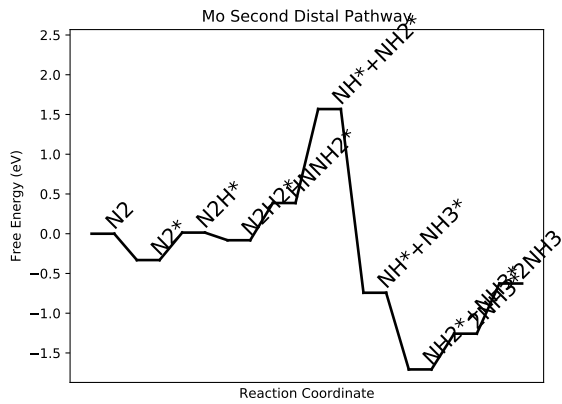


Figure S100: Free energy diagram for Mo

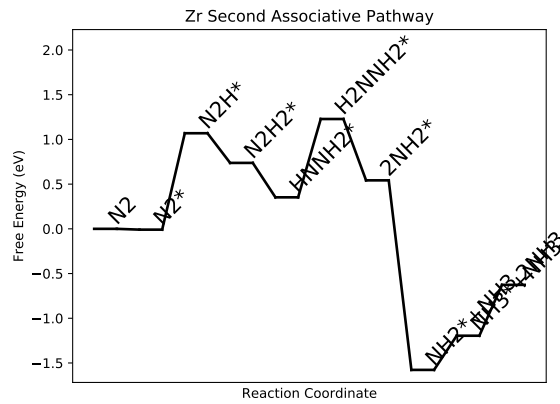


Figure S102: Free energy diagram for Zr

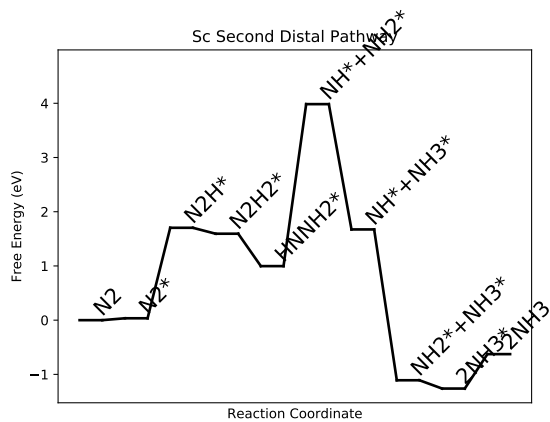


Figure S101: Free energy diagram for Sc

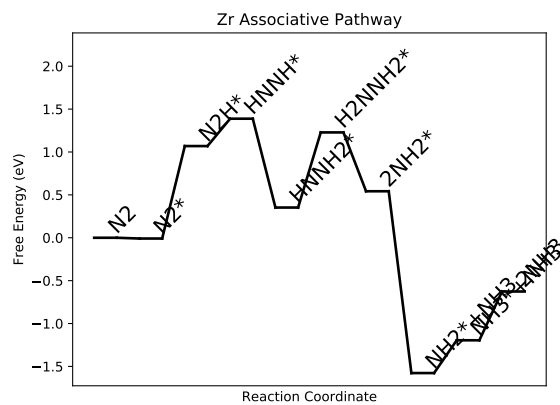


Figure S103: Free energy diagram for Zr

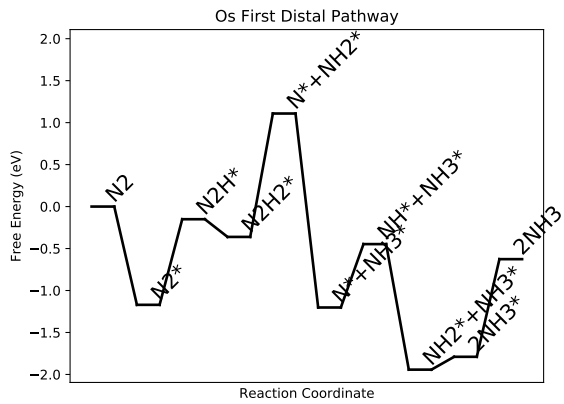


Figure S104: Free energy diagram for Os

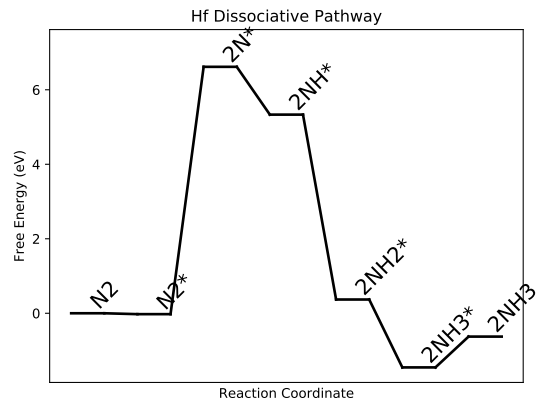


Figure S106: Free energy diagram for Hf

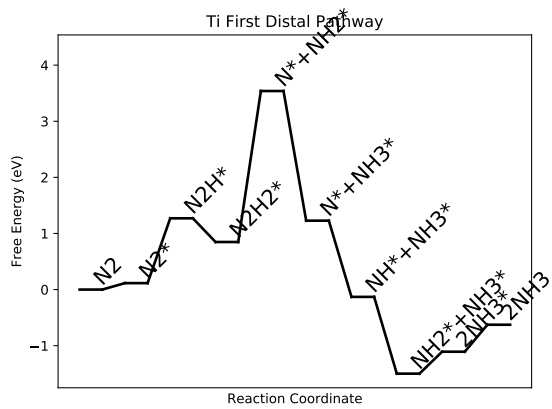


Figure S105: Free energy diagram for Ti

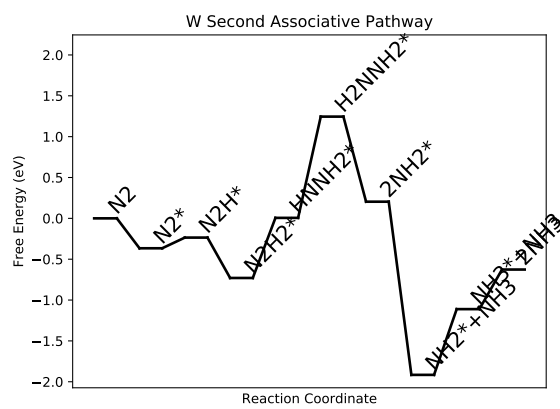


Figure S107: Free energy diagram for W

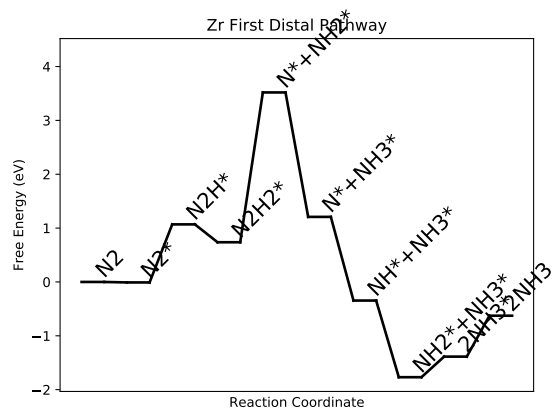


Figure S108: Free energy diagram for Zr

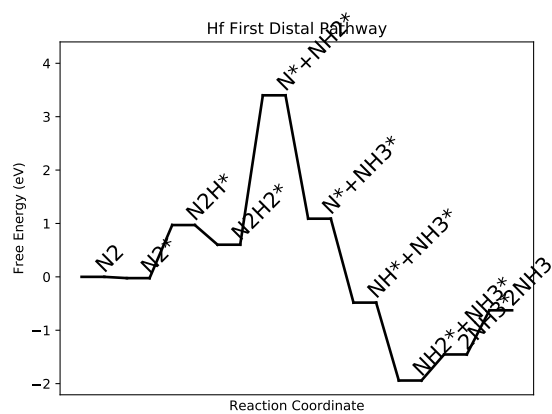


Figure S109: Free energy diagram for Hf